https://doi.org/10.1016/j.engstruct.2020.110911

Investigations into Residual Stresses in S690 Cold-formed Circular Hollow Sections due to Transverse Bending and Longitudinal Welding

Yi-Fei Hu[1,2] , Kwok-Fai Chung[1,2*], Huiyong Ban[3] and David A. Nethercot[4]

[1]*Department of Civil and Environmental Engineering,*
The Hong Kong Polytechnic University, Hong Kong SAR, China.
[2] *Chinese National Engineering Research Centre for Steel Construction (Hong Kong Branch)*
The Hong Kong Polytechnic University, Hong Kong SAR, China.
[3] *Department of Civil Engineering, Tsinghua University, China.*
[4] *Department of Civil and Environmental Engineering, Imperial College London, U.K.*
* *Corresponding author: kwok-fai.chung@polyu.edu.hk*

ABSTRACT

This paper presents an experimental and numerical investigation into residual stresses of S690 cold-formed circular hollow sections (CFCHS) due to transverse bending and longitudinal welding. It is generally expected that adverse effects of residual stresses on both cross-section and member resistances in the S690 CFCHS are proportionally less pronounced, when compared with those in S355 CFCHS owing to increased yield strengths of the steels. Hence, there is a need to determine the distribution of residual stresses in the S690 CFCHS through a rational experimental and numerical investigation in order to provide accurate data for subsequent structural assessment on these sections.

A total of four S690 CFCHS are fabricated with 6 mm thick plates with i) transverse bending, and ii) longitudinal welding. Surface temperature history at selected positions of these sections are measured with thermocouples during welding while surface residual stresses are measured with the sectioning method after welding. Owing to various practical constraints in measuring residual stresses of these sections accurately, a total of three coordinated finite element models are established in which their numerical results are integrated for rational analyses. The transverse bending process is simulated with two-dimensional models with plane-strain elements which undergo extensive plastic deformations to generate residual stresses after springback. The longitudinal welding process is simulated with two coupled three-dimensional models with solid elements to perform a sequentially-coupled thermomechanical analysis in the presence of those residual stresses due to transverse bending. Consequently, a rational distribution of the residual stresses due to both transverse bending and longitudinal welding in these sections are readily determined with these coordinated finite element models after careful calibration against measured data.

Keywords:

Residual stresses; high strength steels; cold-formed circular hollow sections; bending; welding; thermomechanical analysis.

1. Introduction

Residual stresses may be regarded as inherent initial imperfections in structural steel members, and they are always generated during various fabrication processes, namely, flame cutting, cold bending, press braking, hot rolling, and welding. Residual stresses often cause early yielding in various parts of these structural members, and hence, significant reductions in both strengths and stiffness of these members are common.

Owing to advances in metallurgical development and steel-making technology in the last thirty years, high strength steels with yield strengths at 690 and 960 N/mm^2, i.e. S690 and S960 steels, respectively, are produced regularly in many modern steel mills in the world. Effective use of these high strength steels is generally believed to have tremendous impacts on the construction industry as significant savings in the amounts of the steels become possible: only a half or even one third of the steel tonnages are needed in providing same resistances of those structural members made of normal strength S355 steels. Many structural engineers are eager to explore opportunities of applying these high strength steels to build both heavily loaded and large spanning structures.

1.1 Measuring techniques on residual stresses

During the past fifty years, a large number of experimental investigations were carried out to examine residual stresses in fabricated structural members of S235 and S355 steels. Rossini et al. [1] summarized different measurement techniques for residual stresses, and compared both advantages and disadvantages of each method, in particular, both the penetration and the spatial resolution of each of these techniques. In general, most of the residual stress measurements on steel sections were obtained with the use of the sectioning method and the hole-drilling method as these two methods were relatively simple to execute. Experimental results of residual stresses on steel sections with the hole-drilling method were presented by several researchers [2,3,4], and this method was incorporated into ASTM [5] as a standard procedure for residual stress measurements in 2011.

As the hole drilling method was rather difficult to be applied in curved surfaces to achieve accurate results, the sectioning method was widely adopted in measuring residual stresses in circular hollow sections as well as in rectangular hollow sections with small dimensions, as reported in Tebedge et al. [6] and Rossini et al. [1]. Residual stresses in cruciform, I- and box sections fabricated from high strength steel plates with a nominal yield strength of 690 N/mm^2 were also measured by Rasmussen & Hancock [39,40]. Strain gauges were attached onto both the outer and the inner surfaces of the steel sections, and wire-cutting was employed to cut out a series of steel strips from the sections. Hence, in each steel strip, the internal residual stresses were released through both stretching and bending of the steel strips, and these deformations were readily registered in the strain gauges. It should be noted that through thickness distributions of the residual stresses could not be measured with these strain gauges. In many cases, the residual stresses were assumed to vary linearly across the plate thicknesses [7,8,9,10,11,12,13,14] though non-linear distributions were reported in some theoretical investigations [3,7]. Although Whittemore gauges and curvature dials were used from time to time in the residual stress measurements, accuracy of the measured values was somehow unwarranted [13]. In general, the major challenge in applying the sectioning method is the difficulty in measuring residual stresses accurately in those steel strips attached with weldments as i) residual stresses vary considerably across the widths of these strips, and ii) the cross-sectional shapes and sizes of these weldments are often difficult to be controlled. Errors in these values often lead to problems in establishing the magnitudes of these tensile residual stresses, and hence, force equilibrium of the cross-sections.

1.2 Numerical investigations into residual stresses of welded sections

In order to determine welding-induced residual stresses in the steel sections during fabrication, computational welding mechanics [15] was developed in the 1990's to simulate both thermal and mechanical responses of the steel sections under direct exposure of a heat source. In general, three dimensional finite element models were employed in order to obtain accurate values of both temperatures and residual stresses [4,16,17]. It should be noted that:

a) As the heat transfer formulation for radiation, convection and conduction is well established, an accurate prediction of the transient temperature history in the steel sections during welding requires an effective representation of the moving welding arc. A double ellipsoidal model [18] is widely adopted as the heat source model in the three-dimensional finite element models in which the heat energy is distributed into the front and the rear hemispheres of the double ellipsoid unequally. Hence, with properly selected values for specific welding procedures, the volumetric heat flux of the heat source model is readily simulated, and the thermal responses of the steel sections are readily predicted.

b) For thermomechanical analyses of welding-induced residual stresses, it is essential to adopt accurate thermal properties of the steels such as heat capacity, conductivity and linear expansion over a wide range of temperatures. Accurate full-range stress-strain curves of the steels at elevated temperatures under both transient and steady states [19,20] are also required. Moreover, the support conditions of the finite element meshes should be properly modelled for accurate prediction in the mechanical responses of the steel sections.

Over the past thirty years, a number of researchers developed various advanced finite element models to simulate the welding processes in steel sections, and many of these models had been calibrated against complementary test data. In general, the residual stresses in S275 and S355 welded H- and box sections of a wide range of practical dimensions had been extensively examined. A detailed investigation into residual stresses in both welded T-joints and Y-joints between high strength

RQT701 steel plates (with a yield strength at 690 N/mm^2) was reported by Lee et al. [16], and sequentially coupled thermal-stress analyses were conducted to assess effects of different welding sequences onto the residual stresses induced within the joints. Moreover, a comprehensive experimental and numerical investigation into the residual stresses of a total of four S690 welded H-sections of different sizes and plate thicknesses was reported by the authors [4]. The through-thickness distributions of the residual stresses in the vicinity of the flange/web junctions were thoroughly examined with the use of advanced coupled thermomechanical analyses. Owing to the presence of large temperature variations within the junctions during welding, the residual stresses were found to be highly non-linear, and hence, the weighted averages of the residual stresses over the thicknesses of the flanges and the webs of the welded H-sections were found to be significantly smaller than generally anticipated.

However, a review in the literature reveals that experimental investigations into residual stresses in high strength S690 steel cold-formed hollow sections are rather limited as systematic measurements on residual stresses in these sections with different transverse bending and longitudinal welding processes are often found to be prohibitively laborious and time-consuming. In general, it is unsure whether those residual stress distributions reported in the literature for S355 cold-formed hollow sections are readily applicable to S690 cold-formed hollow sections with similar shapes and sizes.

1.3 Objectives and scope of work

In order to enable effective use of high strength S690 steels in construction, a comprehensive research and development programme into mechanical properties of S690 steels and structural behaviour of S690 fabricated sections was undertaken at the Chinese National Engineering Research Centre for Steel Construction (Hong Kong Branch) of the Hong Kong Polytechnic University. It is considered essential to investigate effects of two common fabrication processes, namely, i) transverse bending, and ii) longitudinal welding onto both the mechanical properties and the structural behaviour of S690 cold-formed circular hollow sections (CFCHS). It is generally expected that adverse effects of residual stresses on both cross-section and member resistances in the S690 CFCHS are proportionally less pronounced, when compared with those in S355 CFCHS owing to increased yield strengths of the steels. Hence, there is a need to establish accurate residual stress distributions in the S690 CFCHS through a scientific experimental and numerical investigation in order to provide accurate data for subsequent structural assessment on the S690 CFCHS,

This paper describes an experimental and numerical investigation into the residual stresses in the S690 CFCHS, and the following tasks are carried out:

- Experimental investigation

A total of 4 CFCHS, namely Sections C1 and C1-nw, and Sections C2 and C2-nw, as shown in Figure 1, are fabricated from S690 steel plates with a nominal thickness of 6 mm. It should be noted that Sections C1-nw and C2-nw are fabricated with transverse bending only, i.e. without welding while Sections C1 and C2 are fabricated with both transverse bending and longitudinal welding. Surface temperature history at specific locations of Sections C1 and C2 are measured with thermocouples during welding for subsequent data analyses. Strain gauges are installed in Sections C1-nw and C1 as well as Sections C2-nw and C2 so that longitudinal residual stresses at both the outer and the inner surfaces of these Sections are measured through the sectioning method. By rational analyses on the measured data, both the outer and the inner residual stress distributions of these Sections due to i) transverse bending, and ii) longitudinal welding are obtained.

- Numerical investigation

  In order to predict residual stresses in these S690 CFCHS accurately, a total of three coordinated finite element models are established in which their numerical results are integrated for rational analyses. The finite element package ABAQUS is employed for numerical investigations [38] in this study. The transverse bending process is simulated with two-dimensional models with plane-strain elements which undergo extensive plastic deformations to generate residual stresses after springback. The longitudinal welding process is simulated with two coupled three-dimensional models with solid elements to perform a sequentially coupled thermomechanical analysis in the presence of those residual stresses due to transverse bending. Calibration of the models against i) the measured temperature history during welding, and ii) the measured residual stresses after welding are also carried out.

Table 1 summarizes the key activities of the present investigation. Key areas of interest of the present investigation are:

- to provide experimental data on i) surface temperature history during welding, and ii) surface residual stresses after welding of the sections;
- to develop advanced finite element models with appropriate thermal and mechanical parameters and properties for accurate prediction of both temperatures and residual stresses of the sections; and
- to assess residual stress distributions along the perimeters and their variations across the plate thicknesses of the sections.

All the S690 steel plates adopted in the present investigation are 6.0 mm thick, and they are manufactured to EN 10025: Part 6 [21] which requirements on both chemical compositions and mechanical properties are presented in Tables 2 and 3. It should be noted that all the CFCHS are fabricated in a qualified manufacturer with highly experienced technical staff, as illustrated in

Figure 2. In general, all the plates are cut into suitable sizes from the parent steel plates through the use of a plasma cutting technique. The edges of these plates are bent locally using a press-braking machine. After that, these plates with pre-bent edges are bent transversely by a three-roller bending machine at various locations along their lengths to form circular sections of specific diameters. Finally, longitudinal welding is performed by a qualified welder using a gas metal arc welding (GMAW) method according to common welding practice. The welding electrode ER110S-G (with a diameter of 1.2 mm) to AWS A5.28 [22] is employed. Both the chemical compositions and the mechanical properties of the welding electrode is also presented in Tables 2 and 3 for easy comparison.

It is well known that the S690 steels achieve their greater strengths through heat treatment, such as Quenching and Tempering, and these benefits may be reduced significantly if these QT steels are subsequently welded without a proper control on the heat input energy during welding. Refer to the literature [23,24,25,26] for details.

2. Experimental investigations

A total of four CFCHS are fabricated with the transverse bending and the longitudinal welding processes. Surface temperature history at specific locations of Sections C1 and C2 are measured with thermocouples during welding, and residual strains at both the outer and the inner surfaces of Sections C1 and C1-nw as well as Sections C2 and C2-nw are measured through sectioning after welding. Details of these investigations are described as follows.

2.1 Material properties

In order to obtain basic mechanical properties of the S690 steel plates with a nominal thickness of 6.0 mm, a series of standard tensile tests are carried out according to BS EN ISO-6892-1[27]. A total of three rectangular coupons are tested, and typical dimensions of these coupons are shown in Figure 3a). The tensile tests are conducted with a Servo Hydraulic Fatigue Testing System, as shown in Figure 3b), and the loading capacity of the testing system is 500 kN. An extensometer with a gauge length of 25.000 mm is mounted onto the coupons to measure their strains throughout testing, as shown in Figure 3c). It should be noted that in order to measure full range deformations of the coupons, a digital photo analysis (DPA) [28] is adopted to measure their instantaneous deformations according to changes in pixels in high resolution digital photos taken at close intervals throughout the tests.

After data analyses on these digital photos, the full-range engineering stress-strain curves of all these three coupons are plotted in Figure 4a) while their measured mechanical properties are summarized in Table 3. It should be noted that in EN 1993-1-12 [29], the following requirements for high strength steels up to Grade S700 are specified as follows:

i) $f_u / f_y \geq 1.05$,

ii) $\varepsilon_u \geq 15f_y / E$, and (1)

iii) $\varepsilon_f \geq 10\%$

where

f_y	is the yield strength of the steel;
f_u	is the tensile strength of the steel;
ε_u	is the elongation corresponding to the tensile strength; and
ε_f	is the elongation at fracture.

Based on the test results summarized in Table 3, it is found that the mechanical properties of the S690 steel plates are highly consistent, and all the S690 steel plates adopted in this study are shown to satisfy these requirements. It should be noted that the measured yield strengths range from 722 to 729 N/mm^2 while the nominal yield strength of the welding electrode is 720 N/mm^2. Through the use of a set of widely accepted transformation formulae, the corresponding true stress–strain (σ_t - ε_t) curve of the S690 steel plates, as shown in Figure 4b), is adopted in all subsequent finite element analyses.

2.2 Temperature measurements during welding

In order to measure surface temperature history continuously during welding of the S690 CFCHS, a total of 6 Type-K thermocouples are attached to specific locations in the vicinity of the welding seams on the outside surfaces of each of the two sections, namely Sections C1 and C2. As shown in Figure 5, they are 100 mm apart in the longitudinal direction, and 10 mm apart in the transverse direction. HT putty is employed to isolate exposed surfaces of these thermocouples from the air so that temperature measurement is not interfered by heat convection nor radiation. Hence, their temperatures are measured only through direct heat conduction. It should be noted that accuracy of these thermocouples is ± 1.5°C, and their maximum working temperature is 1200°C.

In both Sections C1 and C2, single-V weld seams are prepared at the edges of the steel plates, and ceramic backings are attached at the underside of the weld seams, as shown in Figure 6. A two-pass welding procedure is adopted to control the heat input energy during welding. All the welding parameters, including current, voltage and welding speed, are carefully controlled and recorded during welding, and key values of these parameters are summarized in Table 4.

2.2.1 Measured surface temperature history

The surface temperature history of Sections C1 and C2 obtained from the thermocouples are plotted in Figure 7. It is show that

- The measured temperatures of the first group of thermocouples, namely, T1, T3 and T5, which are 10 mm away from the welding seam, are found to increase sharply when the heat source approaches. After reaching the maximum values at about 400 to 475 ^{o}C, the temperatures of these thermocouples drop approximately to 150 °C after about 250 to 300 s.

- The measured temperatures of the second group of thermocouples, namely, T2, T4 and T6, which are 20 mm away from the weld seam, are found to have relatively lower maximum temperatures, when compared with those of the first group of thermocouples. After reaching the maximum values at about 250 to 300 ^{o}C , the temperatures of these thermocouples drop approximately to 150 °C after about 300 to 350 s.

The maximum temperatures measured by various thermocouples in both Sections C1 and C2 are summarized in Table 5. It should be noted that both the welding parameters and the surface temperature history of Sections C1 and C2 recorded during welding are considered to be important measured data for subsequent calibration of these finite element models presented in the following sections.

2.3 Residual stress measurements after welding

Both Sections C1 and C1-nw as well as both Sections C2 and C2-nw are employed for residual stress measurements. As shown in Figure 8, each of these CFCHS is cut with cold-sawing into three parts of different lengths, i.e. 150, 260 and 250 mm, and sectioning is performed in the CFCHS with a length of 260 mm. As the distribution of the residual stresses are assumed to be symmetrical along the weld seams of the CFCHS, only half of each of the CFCHS is used for strain measurements. The width of each longitudinal strip is 10.0 ±0.1 mm, and strain gauges are attached to both the outer and the inner surfaces at the mid-length of each strip, as shown in Figure 9. It should be noted that waterproof glue is applied carefully to protect all the strain gauges before cutting, and a coolant is applied during the cutting process in order to minimize any heat generated. All the deformed strips of both Sections C1-nw and C1 after wire cutting are shown in Figure 9.

2.3.1 Measured residual strains

Strain readings prior to and after the wire-cutting are recorded. Residual strains on both the outer and the inner surfaces, ε_o and ε_i , respectively, are calculated by subtracting the initial measured strains from the final measured strains. In general, the corresponding residual stresses, σ_o and σ_i , are determined from the measured strains according to the Hook's Law, as shown in Equation 2:

$$\sigma_o = -E \cdot \varepsilon_o \quad ; \quad \sigma_i = -E \cdot \varepsilon_i \qquad (2)$$

where

E is the measured elastic modulus of the steel.

The residual stresses of both the outer and the inner surfaces, σ_o and σ_i , of all the strips of each of the sections are presented in Tables 6 to 9. It should be noted that all of these are longitudinal residual stresses of the sections, and a positive value indicates a tensile residual stress while a negative value indicates a compressive residual stress. The measured residual stress distributions on both the outer and the inner surfaces of the sections for $0^o < \theta < 180^o$ are plotted in Figure 10. It should be noted that

a) For Section C1-nw, the outer residual stresses σ_o are found to be tensile while the inner residual stresses σ_i are found to be compressive. The values of both σ_o and σ_i are almost equal but opposite to each other when θ exceeds 15^o, and the magnitudes of both of them remain to be fairly constant at about 209 N/mm^2 when θ ranges from 15 to 180^o . However, the magnitudes of both σ_o and σ_i reduce linearly to zero when $\theta = 0^o$, i.e. at the free edge. Similar results are also found in Section C2-nw.

b) For Section C1, both the outer residual stress σ_o and the inner residual stress σ_i are found to be highly tensile in the close vicinity of the welding seams, i.e. when θ is about 0^o. This is well explained with the presence of very high temperatures during welding, and hence, large locked-in tensile stresses are induced after welding. However, when θ increases to about 15^o, σ_o decreases sharply to about 100 N/mm^2 while σ_i decreases further to a compressive stress of about 300 N/mm^2. As θ increases further, both σ_o and σ_i increase steadily, and they become almost equal but opposite to each other once θ exceeds 60^o. Then, the values of both σ_o and σ_i are typically 200 N/mm^2 when $60^o \leq \theta \leq 180^o$.

Similar results are also found in the residual stress distribution of both Sections C2-nw and C2.

3. Numerical investigations

In order to simulate effects of both the transverse bending and the longitudinal welding processes on the S690 CFCHS, a total of three coordinated finite element models are established in which their numerical results are integrated for rational analyses. An overview of the series of numerical investigations is presented in Figure 11 while details of the finite element modelling are described as follows.

a) Transverse bending

Two-dimensional models with plane-strain elements are established to simulate the transverse bending process on Sections C1-nw and C2-nw, and the models undergo large deformations with extensive plastic deformations in the elements to give residual stresses induced along the perimeters of the sections as well as across their thicknesses after springback.

b) Longitudinal welding

Two coupled three-dimensional models with solid elements are established to perform sequentially-coupled thermomechanical analyses to simulate the longitudinal welding process on Sections C1-nw and C2-nw in the presence of the residual stresses due to transverse bending. These are two-stage analyses, namely, i) heat transfer analysis, and ii) thermomechanical analysis, and they are carried out sequentially in these sections to determine their welding-induced thermal and mechanical responses. After completion of these numerical analyses, these two sections become numerical Sections C1 and C2 , respectively.

3.1 Transverse bending

Transverse bending is simulated using two-dimensional finite element models in which a steel plate is bent numerically with three rollers into an open circular hollow section, and two-dimensional plane-strain elements CPE4R with reduced integration and hourglass control are employed. A typical model together with the boundary conditions is shown in Figure 12. It should be noted that after inserting the steel plate into position, the acting roller moves down to bend the steel plate, and then the rollers rotate in opposite directions to feed the steel plate for roll-bending. Hence, the steel plate is bent with a constant curvature with extensive plastic deformations to form an open circular hollow section. Upon release of the acting roller, springback in the open circular hollow section takes place. Both geometrical and material nonlinearities are incorporated into the model, and the von Mises criterion is adopted to capture yielding in the steel plate. The true stress-strain curve obtained from standard tensile tests, as shown in Figure 4b), is adopted. Isotropic hardening rule is applied for steel in the finite element models.

3.1.1 Mesh convergence study

A mesh convergence study on transverse bending of Section C1-nw is performed, and a total of three meshes with different numbers of layers of elements across the plate thickness are considered. Figure 13 plots the variations of both the longitudinal and the transverse residual stresses of the sections when 4, 8 and 12 layers of elements are adopted. Comparison among these residual stress variations is also illustrated in Figure 13. It is shown that convergence is established as the residual stresses in both the meshes with 8 and 12 layers of elements are found to be very close to one another. Moreover, the predicted residual stress distributions are found to be broadly similar to the simplified analytical solutions reported by Moen et al. [30] and those derived by the authors [31], as shown in Figure 14.

3.1.2 Predicted longitudinal residual stresses due to transverse bending

After establishing mesh convergence study, the predicted residual stresses of both Sections C1-nw and C2-nw have been evaluated successfully, and they are plotted onto the graph of the measured residual stresses in Figure 10a) for direct comparison. It is shown that both the predicted and the measured residual stresses of each of these two sections are similar in pattern though their magnitudes differ by a factor of about 1.06 to 1.45 throughout the perimeters of the sections.

3.2 Longitudinal welding

The following two coupled three-dimensional models are established to simulate the longitudinal welding process to predict residual stresses induced onto the perimeters of the sections:

- A three-dimensional model is established with three-dimensional heat transfer elements DC3D8 to predict thermal responses along the free longitudinal edges of the sections under a welding arc. Deposition of molten materials of the welding electrode in each welding run is simulated using a "Birth and Death" technique while temperature history of the sections in both heating up and cooling down phases of the welding process are predicted. These temperature history data at specified points of the sections are compared with the measured temperature history data presented in Section 2.2 for calibration of the heat transfer analysis. It should be noted that these predicted temperature history data are adopted as input temperatures of the sections for subsequent thermomechanical analyses.

- Based on various physical and mechanical properties of the steels at elevated temperatures, another three-dimensional model is established with three-dimensional stress elements C3D8R to predict mechanical responses of the sections subjected to the predicted temperature history obtained from the heat transfer models. The predicted residual stresses due to welding on both the outer and the inner surfaces of the sections are compared with the measured residual stresses presented in Section 2.3 for calibration of the thermomechanical analyses.

Details of finite element models and various aspects of the sequentially-coupled thermomechanical analyses are described as follows.

3.2.1 Finite element models

Figure 15 shows an overall view of the three-dimensional model of the CFCHS which is properly supported during non-linear analyses. It should be noted that both heat transfer element DC3D8 and thermomechanical element C3D8R are highly efficient elements as there is only one integration point at their centroids. Hence, they require minimum computational resources in terms of memory and time. According to experiences in similar modelling [4,32], the potential problem of hour-glass fictitious deformation is readily eliminated with the use of at least 4 elements across the plate thickness. It should be noted that all the residual stresses due to transverse bending, as shown in

Figure 13 and described in Section 3.1, are fully incorporated into the models as initial stresses at the integration points of the elements.

3.2.2 Material and mechanical properties at elevated temperatures

The true stress–strain (σ_t - ε_t) curve shown in Figure 4b) is adopted as the material model of the S690 steels. Moreover, various temperature-dependent material properties, namely, thermal conductivity, specific heat capacity and thermal expansion coefficient as well as reduction factors to yield strength and Young's modulus given in EN 1993-1-2 [33] are adopted in the present study, and their variations with temperatures are illustrated in Figure 16. According to a number of literature[4,33], the radiation emissivity ξ_{res} may be taken as 0.5 while the film coefficient α for radiation may be taken as 15 W/m^2/K.

3.2.3 Heat source model

The double ellipsoidal shown in Figure 17 is employed to simulate the moving welding arc [2, 4], and the volumetric heat flux of the double ellipsoid, q_f and q_r , are defined with a total of four geometric parameters (or semi-axes), namely, a_1 , a_2 , b and c [18] as follows:

$$\begin{cases} q_f\left(x,y,z\right) = \dfrac{6\sqrt{3}f_f Q}{a_1 bc\pi\sqrt{\pi}}\exp(-\dfrac{3x^2}{a_1^2})\exp(-\dfrac{3y^2}{b^2})\exp(-\dfrac{3z^2}{c^2}) \\ q_r\left(x,y,z\right) = \dfrac{6\sqrt{3}f_f Q}{a_2 bc\pi\sqrt{\pi}}\exp(-\dfrac{3x^2}{a_2^2})\exp(-\dfrac{3y^2}{b^2})\exp(-\dfrac{3z^2}{c^2}) \end{cases} \quad (3)$$

where

q_f and q_r	the volumetric heat flux corresponding to the front and the rear hemi-spheres, respectively [W/m^3];
Q	is the total heat input energy of the heat source [J];
x, y and z	are the local coordinates as shown in Figure 17; and
f_f and f_r	are fractions illustrating energy distribution.

Based on experience of the authors on similar investigations [18,34], the values of these four geometric parameters of the double ellipsoidal are specified according to the following:

i) the total heat input energy, Q , of the heat source during welding which is determined as $\eta \cdot U \cdot I$ according to various welding parameters given in Table 4;
ii) the corresponding size and shape of the molten materials of the welding electrode in each welding pass; and
iii) differences between the predicted and the measured temperatures at specific locations of the sections.

All those values of parameters a_1, a_2, b, and c of the heat source model for both Sections C1 and C2 presented in Figure 17 should be adopted as they have been calibrated for GMAW, and the corresponding welding efficiency, η, should be taken as 0.85 [4, 35]. Moreover, the values of both f_f and f_r of the heat source model should be taken as 0.6 and 1.4, respectively, and their sum is equal to 2.0.

3.2.4 Mesh convergence study

Three meshes with different configurations and degrees of refinement are established, and they are illustrated as Meshes A, B and C for easy comparison in Figure 18. As highly localized stresses are expected to be generated during the longitudinal welding processes, the meshes in the vicinity of the welding seams are successively refined in these meshes. Key information of these meshes are summarized in Table 10. While the mesh sizes are steadily reduced from 15 mm to 10 mm, and then to 5 mm in Meshes A, B and C, the total numbers of elements in these meshes are 6,720, 14,688 and 76,032 , respectively.

The aspect ratio of each finite element mesh, i.e. the ratio of the longest edge length to the shortest edge length, should not exceed certain limits in order to ensure numerical accuracy during analyses. The aspect ratios of Meshes A, B and C are found to be 10.0, 6.7 and 5.0, respectively, and these are considered to be acceptable [38].

Both the heat transfer analyses and the thermomechanical analyses of the sequentially-coupled thermomechanical models with Meshes A, B and C have been successfully completed. The surface temperatures and the surface residual stresses in the vicinity of the welding seams of these models are plotted in Figure 19 for easy comparison. A sectional view of the welding seam for each mesh is also provided to illustrate the maximum temperature distributions during welding. It should be noted that the grey region in the sectional view represents the molten materials of the welding electrode with a temperature above 1500 °C while only very small temperature differences are apparent within the welding seams.

Figure 20 illustrates the numerical results of both the heat transfer analyses and the thermomechanical analyses of the sequentially-coupled thermomechanical models with Meshes A, B and C. It is shown that from Meshes A to C, the surface temperatures at the location of Thermocouple T03 decrease steadily from 471˚C to 456˚C. Moreover, the corresponding maximum residual stresses at the outer surface decrease from +755 to +749 N/mm^2 while the corresponding maximum residual stresses at the inner surface decrease from +934 to +869 N/mm^2. Hence, convergence in the numerical results among these meshes is achieved, and Mesh B is considered to be adequately accurate and computational efficient for all subsequent analyses.

3.2.5 Finite element results

Non-linear analyses of both the heat transfer and the thermomechanical models with Mesh B for Sections C1 and C2 have been carried out. Both the temperatures and the residual stresses of Sections C1 and C2 have been evaluated successfully, and they have been calibrated carefully against both the measured surface temperature history and the measured surface residual stresses obtained in the experimental investigation.

a) Temperature history

Figure 21a) illustrates the predicted transient surface temperature distributions of both Sections C1 and C2 during welding obtained from the heat transfer models. The predicted surface temperatures at various locations of Thermocouples T1 to T6 induced by two different weld runs of each of the Sections are plotted in Figure 7 for direct comparison with the corresponding measured temperatures. It is evident that the predicted surface temperatures compare very well to those corresponding measured values.

Moreover, the predicted maximum surface temperatures in both Sections C1 and C2 are summarized in Table 5 for direct comparison with those measured values. In general, it is shown that a good agreement between both the predicted and the measured maximum surface temperatures is established. It should be noted that the predicted temperatures are found to be 12.3 and 16.6% larger than those measured temperatures for Sections C1 and C2, respectively. These temperatures tend to be over-estimated with an average margin of 14.4% so that conservative residual stresses are predicted subsequently.

b) Residual stress distribution

Figure 21b) presents an overview of the numerical results of the thermomechanical analysis of each of Sections C1 and C2 in a graphical manner while the surface residual stresses are plotted onto the graphs of the measured values in Figure 10b) for direct comparison. It is apparent that these predicted residual stresses compare very well with the measured values throughout the entire perimeters of the two sections.

In order to demonstrate effectiveness of both the transverse bending models and the longitudinal welding models, Tables 6 to 9 present direct comparison on the measured and the predicted residual stresses of Sections C1-nw and C2-nw as well as Sections C1 and C2. It is shown that

- For Sections C1-nw and C2-nw, the average differences between the predicted and the measured surface residual stresses due to transverse bending are found to range from 52 to 62 N/mm^2. The maximum error is 30% when compared with the average measured residual stress, and 8.5% when compared with the measured yield strength of the steels.

- Similarly, for Sections C1 and C2, the average differences between the predicted and the measured residual stresses due to longitudinal welding and transverse bending are found to range from 12 to 48 N/mm^2. The maximum error is 26% when compared with the average predicted residual stress, and 6.6% when compared with the measured yield strength of the steels.

In general, the errors obtained from the above data analyses are found to be well within the acceptable error ranges reported by many other researchers in the literature [10,12,14]. Hence, both the transverse bending models and the longitudinal welding model are considered to be highly effective in simulating both processes.

Figure 22 plots cross-sectional distributions of the predicted longitudinal residual stresses in both Sections C1-nw and C2-nw due to transverse bending. The residual stresses increase linearly from 0 when $\theta = 0^o$ to about ±100 N/mm^2 when $\theta = 15^o$ at both the outer and the inner surfaces. After that, the residual stresses reach ±150 N/mm^2, and the magnitudes remain almost constant when $20^o \leq \theta \leq 180^o$. Refer to the through-thickness plots of their residual stresses at specific locations with $0^o \leq \theta \leq 180^o$.

Figure 23 plots cross-sectional distributions of the predicted longitudinal residual stresses in both Sections C1 and C2 due to longitudinal welding. Large tensile residual stresses are evident in the vicinities of the weld seams while there are both tensile and compressive residual stresses over the plate thicknesses in the rest of the perimeters of the sections. Refer to detailed plots of their through-thickness variations at specific locations with $0^o \leq \theta \leq 180^o$. It should be noted that:

- At Section A-A where $\theta = 0^o$, large tensile residual stresses are developed owing to longitudinal welding, i.e. these large tensile stresses are caused by solidification of the welding electrode during cooling down from high temperatures, and hence, the through-thickness stress distribution is fairly uniform. Similar observations are also found in both Sections B-B and C-C where $\theta = 5^o$ and 10^o, respectively, though the magnitudes of these residual stresses decrease sharply.

- At Section D-D where $\theta = 15^o$, as the magnitudes of the tensile residual stresses due to longitudinal welding decrease significantly, both the tensile and the compressive residual stresses due to transverse bending become relatively dominant. Hence, the through-thickness stress distribution is rather asymmetrical.

- From Sections E-E to I-I where $20^o < \theta \leq 180^o$, the through-thickness stress distribution is highly asymmetrical owing to both the tensile and the compressive residual stresses due to transverse bending.

Hence, the effects of both transverse bending and longitudinal welding onto the residual stress distributions of the sections are clearly identified and illustrated.

c) Self-equilibrium of residual stresses

It is important to establish force equilibrium of the residual stresses in each of Sections C1 and C2. As shown in Figure 24, all the residual membrane stresses along the perimeters of the sections are summed up over their corresponding elemental areas to give i) a large tensile force which is in the vicinity of the welding seam, ii) a large compressive force over a large portion of the perimeter, and iii) a very small tensile force over the rest of the perimeter. Due to symmetry, only half of the perimeters of the sections are considered. It is found that

- For Section C1, the compressive force is 53.5 kN while the out-of-balance force is -0.2 kN, and hence, this gives a discrepancy at merely 0.4%.

- For Section C2, the compressive force is 47.8 kN while the out-of-balance force is +0.4 kN, and hence, this gives a discrepancy at merely 0.8%.

Hence, the predicted residual stress distributions in these two sections are confirmed to be in self-equilibrium.

Consequently, the proposed three coordinated finite element models are demonstrated to be able to predict both thermal and mechanical responses, i.e. temperature history and residual stress distributions, of these S690 CFCHS with adequate accuracy through sequentially coupled thermomechanical analyses, after successful calibration against measured data.

4 Residual stress patterns

Owing to significant variations in the residual stresses across the plate thicknesses, an equivalent residual membrane stress $\sigma_{res,m}$ is established to quantify effects of stretching in these CFCHS primarily due to longitudinal welding. It is defined as follows:

$$\sigma_{res,m} = \frac{1}{t}\int_{-0.5t}^{+0.5t} \sigma \, dt \qquad (4a)$$

Moreover, an equivalent residual bending stresses $\sigma_{res,b}$ is established to quantify effects of bending in these CFCHS primarily due to transverse bending, and it is defined as follows:

$$\sigma_{res,b} = \frac{6}{t^2}\int_{-0.5t}^{+0.5t} \sigma \cdot t \, dt \qquad (4b)$$

Both the equivalent residual membrane stresses $\sigma_{res,m}$ and the equivalent residual bending stresses $\sigma_{res,b}$ of all the models of Sections C1-nw and C1 as well as Sections C2-nw and C2 are plotted in Figure 25 for direct comparison. Hence, the effects of longitudinal welding in the S690 CFCHS are readily identified by examining the differences of these residual stress distributions. It should be noted that:

For Sections C1-nw and C2-nw,

- the values of $\sigma_{res,m}$ are almost zero throughout the entire perimeters of the sections, i.e. $0^o \leq \theta \leq 180^o$; and
- the values of $\sigma_{res,b}$ are found to increase linearly from zero to about 150 N/mm^2 when $\theta = 15^o$, and then, they remain to be almost constant throughout the rest of the perimeters of the sections, i.e. $15^o \leq \theta \leq 180^o$.

For Sections C1 and C2,

- the values of $\sigma_{res,m}$ are very high, and they are +751 and +742 N/mm^2 (tensile), respectively when $\theta = 0^o$, and their variation may be described as follows:
  - i) they decrease sharply to zero when $\theta = 10^o$,
  - ii) they further decrease linearly to about -100 to -150 N/mm^2 (compressive) when $\theta = 15^o$,
  - iii) they increase back to zero when $\theta = 83^o$,
  - iv) they further increase to about 36 N/mm^2 when $\theta = 100^o$, and then decrease gradually to zero when $\theta = 180^o$; and
- the values of $\sigma_{res,b}$ are found to increase from zero linearly to about 230 N/mm^2 when $\theta = 15^o$, and then, they remain to be almost constant throughout the rest of the sections, i.e. $15^o \leq \theta \leq 180^o$.

4.1 Comparison with existing residual stress models

A number of residual stress models for the S355 CFCHS are available in the literature since 1970s. Based on experimental data reported in the literature, Wagner et al. [36] proposed a bi-linear model to describe the residual stress model in the CFCHS while a multi-linear model is proposed by Chen and Ross [7]. These residual stress models are plotted in Figure 26a) together with the predicted residual membrane stresses of Sections C1 and C2. It is shown that both residual stress models are very different from the predicted stresses.

More recently, a bi-linear model for high strength Q690 CFCHS is reported by Yang et al. [37], and it is plotted in Figure 26b) together with the predicted residual membrane stresses of Sections C1 and C2. It is shown that the bi-linear model is similar to the predicted residual membrane stresses to some extents though it over-predicts the area under tension, i.e. $\theta = 18^o$ when $\sigma_{res,m} = 0$.

In order to provide an expression to describe $\sigma_{res,m}$ for Sections C1 and C2, a multi-linear model, as shown in Figure 26b), is proposed as follows:

$$\frac{\sigma_{res,m}}{f_y} = \begin{cases} 1.0 - 0.1 \cdot \theta & 0 \le \theta \le 10° \\ 0.40 - 0.04 \cdot \theta & 10° < \theta \le 15° \\ -0.244 + 0.00294 \cdot \theta & 15° < \theta \le 100° \\ 0.113 - 0.00063 \cdot \theta & 100° < \theta \le 180° \end{cases} \quad (5)$$

It should be noted that the proposed model achieves self-equilibrium within the cross section as the out-of-balance force is smaller than 1 % of the total tensile force of the cross section.

5. Conclusions

In order to examine the effects of transverse bending and longitudinal welding on residual stresses of the S690 cold-formed circular hollow sections (CFCHS), a systematic experimental and numerical investigation into thermal and mechanical responses in S690 CFCHS with different sizes is carried out. Surface temperature history at selected positions of these sections are measured with thermocouples during welding while surface residual stresses are measured with the sectioning method after welding. Owing to various practical constraints in measuring residual stresses of these sections accurately, a total of three coordinated finite element models are established in which their numerical results are integrated for rational analyses. The transverse bending process is simulated with two-dimensional models with plane-strain elements which undergo extensive plastic deformations to generate residual stresses after springback. The longitudinal welding process is simulated with two coupled three-dimensional models with solid elements to perform coupled sequentially-coupled thermomechanical analyses in the presence of those residual stresses due to transverse bending. Consequently, a rational distribution of the residual stresses due to both transverse bending and longitudinal welding in these sections are readily determined with these finite element models after careful calibration against measured data.

It should be noted that

a) Both surface temperature history and surface residual stresses in the S690 CFCHS have been successfully measured in experiments through the use of thermocouples during welding and the sectioning method after welding. Details of various welding parameters are also recorded. Hence, through proper instrumentation for the longitudinal welding process, accurately measured data are available for careful calibration of the proposed finite element models.

b) A total of three coordinated finite element models have been established to simulate both the transverse bending and the longitudinal welding processes for the S690 CFCHS, and these models have been carefully calibrated with measured data. Hence, the residual stresses generated by these two processes may be readily predicted with high accuracy, and these stresses will be readily adopted for structural assessments of these sections under practical loading and support conditions.

c) Both the measured and the predicted residual stresses of these S690 CFCHS are found to be less severe than those residual stress models of S355 CFCHS reported in the literature. Large and highly localized residual membrane (tension) stresses are induced in the vicinity of the welding seams after welding due to quick solidification of the welding electrode during cooling down. It should be noted that the tension zones (defined by the angle θ) in these S690 CFCHS are significantly smaller in area, when compared with those of the S355 CFCHS due to their increased yield strengths. Based on the carefully calibrated finite element models, a multi-linear model is proposed to describe the residual membrane stresses for subsequent assessments of these S690 CFCHS.

The proposed coordinated finite element models are now ready for parametric studies to generate numerical data for development of a residual stress pattern for the S690 CFCHS with various diameters and thicknesses, and the work will be reported separately.

Acknowledgments

The research work leading to publication of this paper was supported by a comprehensive research and development programme on effective use of high strength S690 steels in construction undertaken at the Chinese National Engineering Research Centre for Steel Construction (Hong Kong Branch) supported by the Innovation and Technology Fund of the Government of Hong Kong SAR and the Research Committee of the Hong Kong Polytechnic University (Project Nos. 1-BBY3 and 1-BBV3). Moreover, the authors are grateful for the research fundings on high strength S690 steelwork awarded by the General Research Funds of the Research Grants Council of the Government of Hong Kong SAR (Project Nos. PolyU 152194/15E, 1526871/16E, 152231/17E and 152157/18). The research studentship provided by the Research Committee of the Hong Kong Polytechnic University to the first author (Project No. RTZX) is also gratefully acknowledged.

Supply of the high strength S690 steel plates by Nanjing Iron and Steel Company Ltd. in Nanjing, and fabrication of cold-formed circular hollow sections by Pristine Steel Fabrication Company Ltd. in Dongguan are also appreciated. Special thanks go to the technicians of the Structural Engineering Research Laboratory at the Hong Kong Polytechnic University during execution of all the tests.

REFERENCES

[1] Rossini, N. S., Dassisti, M., Benyounis, K. Y. & Olabi, A. G. (2012). Methods of measuring residual stresses in components. Materials & Design, 35, 572-588.

[2] Lee, C. K., Chiew, S. P. & Jiang, J. (2012). Residual stress study of welded high strength steel thin-walled plate-to-plate joints, Part 1: Experimental study. Thin-Walled Structures, 56, 103-112.

[3] Tong, L., Hou, G., Chen, Y., Zhou, F., Shen, K. & Yang, A. (2012). Experimental investigation on longitudinal residual stresses for cold-formed thick-walled square hollow sections. Journal of Constructional Steel Research, 73, 105-116.

[4] Liu, X. & Chung, K. F. (2018). Experimental and numerical investigation into temperature histories and residual stress distributions of high strength steel S690 welded H-sections. Engineering Structures, 165, 396-411.

[5] ASTM International. Standard test method for determining residual stresses by hole drilling strain-Gauge Method ASTM E837. West Conshohocken, United States: ASTM International; 2013.

[6] Tebedge, N., Alpsten, G. & Tall, L. (1973). Residual stress measurement by the sectioning method. Experimental Mechanics, 13(2), 88-96.

[7] Chen, W. F. & Ross, D. A. (1977). Test of fabricated tubular columns. Journal of the Structural Division, 103 (ASCE 12809).

[8] Cruise, R. B. & Gardner, L. (2008). Residual stress analysis of structural stainless steel sections. Journal of Constructional Steel Research, 64(3), 352-366.

[9] Ban, H., Shi, G., Shi, Y. & Wang, Y. (2013). Residual stress of 460 MPa high strength steel welded box section: Experimental investigation and modelling. Thin-Walled Structures, 64, 73-82.

[10] Ma, J. L., Chan, T. M. & Young, B. (2015). Material properties and residual stresses of cold-formed high strength steel hollow sections. Journal of Constructional Steel Research, 109, 152-165.

[11] Somodi, B. & Kövesdi, B. (2017). Residual stress measurements on cold-formed HSS hollow section columns. Journal of Constructional Steel Research, 128, 706-720.

[12] Zheng, B., Shu, G. & Jiang, Q. (2019). Experimental study on residual stresses in cold rolled austenitic stainless steel hollow sections. Journal of Constructional Steel Research, 152, 94-104.

[13] Jiao, H. & Zhao, X. L. (2003). Imperfection, residual stress and yield slenderness limit of very high strength (VHS) circular steel tubes. Journal of Constructional Steel Research, 59(2), 233-249.

[14] Shi, G., Jiang, X., Zhou, W., Chan, T. M. & Zhang, Y. (2013). Experimental investigation and

modelling on residual stress of welded steel circular tubes. International Journal of Steel Structures, 13(3), 495-508.

[15] Kim, S. H., Kim, J. B. & Lee, W. J. (2009). Numerical prediction and neutron diffraction measurement of the residual stresses for a modified 9Cr–1Mo steel weld. Journal of Materials Processing Technology, 209(8), 3905-3913.

[16] Lee CK, Chiew SP, Jiang J. (2012). Residual stress study of welded high strength steel thin-walled plate-to-plate joints. Part 2: Numerical modeling. Thin-Walled Structures, 2012; 59: 120–31.

[17] Schmidt, H., & Hattel, J. (2004). A local model for the thermomechanical conditions in friction stir welding. Modelling and simulation in materials science and engineering, 13(1), 77.

[18] Goldak J, Chakravarti A, Bibby M. A new finite element model for welding heat sources. Metall Trans B 1984;15(2):299–305.

[19] Chen, J., Young, B., & Uy, B. (2006). Behavior of high strength structural steel at elevated temperatures. Journal of structural engineering, 132(12), 1948-1954.

[20] Qiang, X., Bijlaard, F., & Kolstein, H. (2012). Dependence of mechanical properties of high strength steel S690 on elevated temperatures. Construction and Building Materials, 30, 73-79.

[21] CEN. BS EN 10025-6, Hot rolled products of structural steels – Part 6: technical delivery conditions for flat products of high yield strength structural steels in the quenched and tempered condition; 2009.

[22] AWS (2005) Specification for Low-Alloy Steel Electrodes and Rods for Gas Shielded Arc Welding. Structural Welding Code – Steel. Miami, United States: American Welding Society.

[23] Liu, X., Chung, K. F., Ho, H. C., Xiao, M., Hou, Z. X., & Nethercot, D. A. (2018). Mechanical behavior of high strength S690-QT steel welded sections with various heat input energy. Engineering Structures, 175, 245-256.

[24] Ho, H. C., Chung, K. F., Huang, M. X., Nethercot, D. A., Liu, X., Jin, H., Nethercot, D. A. & Tian, Z. H. (2020). Mechanical properties of high strength S690 steel welded sections through tensile tests on heat-treated coupons. Journal of Constructional Steel Research, 166, 105922.

[25] Ding, Q., Wang, T., Shi, Z., Wang, Q., Wang, Q., & Zhang, F. (2017). Effect of Welding Heat Input on the Microstructure and Toughness in Simulated CGHAZ of 800 MPa-Grade Steel for Hydropower Penstocks. Metals, 7(4), 115.

[26] Śloderbach, Z., & Pająk, J. (2015). Determination of Ranges of Components of Heat Affected Zone Including Changes of Structure. Archives of Metallurgy and Materials, 60(4), 2607-2612.

[27] BS EN ISO 6892-1 (2009). Metallic materials – Tensile testing: Part 1: Method of test at ambient temperature, British Standards Institution.

[28] Ho, H. C., Liu, X., Chung, K. F., Elghazouli, A. Y., & Xiao, M. (2018). Hysteretic behaviour of high strength S690 steel materials under low cycle high strain tests. Engineering Structures, 165, 222-236.

[29] CEN. (2007). BS EN 1993-1-12, Eurocode 3: Design of steel structures Part 1-12: Additional rules for the extension of EN 1993 up to steel grades S700. European Committee for Standardization.

[30] Moen, C. D., Igusa, T. & Schafer, B. W. (2008). Prediction of residual stresses and strains in cold-formed steel members. Thin-walled structures, 46(11), 1274-1289.

[31] Hu, Y. F., (2019). Structural behaviour of high strength S690 steel cold-formed circular hollow sections, Doctoral dissertation, the Hong Kong Polytechnic University. Hong Kong SAR.

[32]Liu, X., Chung, K. F., Huang, M., Wang, G., & Nethercot, D. A. (2019). Thermomechanical parametric studies on residual stresses in S355 and S690 welded H-sections. Journal of Constructional Steel Research, 160, 387-401.

[33] CEN. (2005). EN-1993-1-2:2005, Eurocode 3: Design of steel structures - Part 1-2: General rules Structural fire design. Brussels, Belgium: European Committee for Standardization.

[34] Goldak JA, Akhlaghi M. Computational welding mechanics. Springer Science & Business Media; 2006.

[35] Singh, R. (2015). Applied welding engineering: processes, codes, and standards. Butterworth-Heinemann.

[36] Wagner, A. L., Mueller, W. H. & Erzurumlu, H. L. (1976). Design interaction curves for tubular steel beam-columns. In Offshore Technology Conference. Offshore Technology Conference, January 1976.

[37] Yang, C., Yang, J., Su, M. & Li, Y. (2016). Residual stresses in high-strength-steel welded circular tube. Proceedings of the Institution of Civil Engineers-Structures and Buildings, 170(9), 631-640.

[38] ABAQUS 6.12. Theory manual. Providence, US: Dassault Systemes Simulia Corp; 2009.

[39] Rasmussen, K. J., & Hancock, G. J. (1992). Plate slenderness limits for high strength steel sections. Journal of Constructional Steel Research, 23(1-3), 73-96.

[40] Rasmussen, K. J., & Hancock, G. J. (1995). Tests of high strength steel columns. Journal of Constructional Steel Research, 34(1), 27-52.

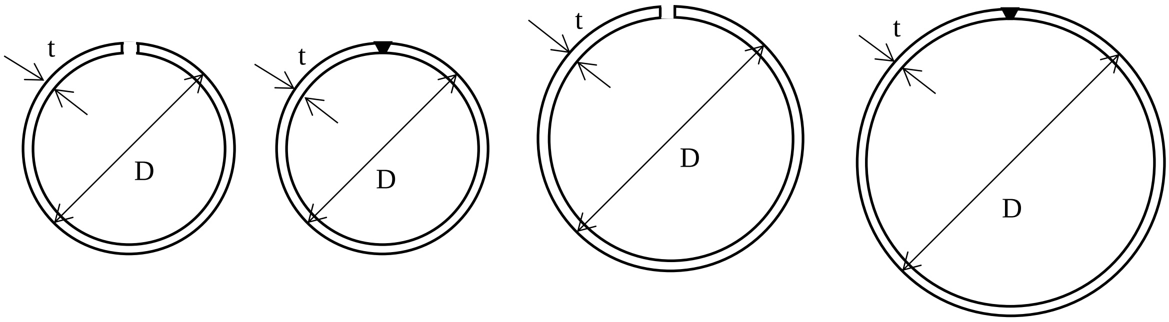

Section C1-nw	**Section C1**	**Section C2-nw**	**Section C2**
D = 150 mm	D = 150 mm	D = 200 mm	D = 200 mm
t = 6 mm	t = 6 mm	t = 6 mm	t = 6 mm

Figure 1 Cross sectional dimensions of CFCHS

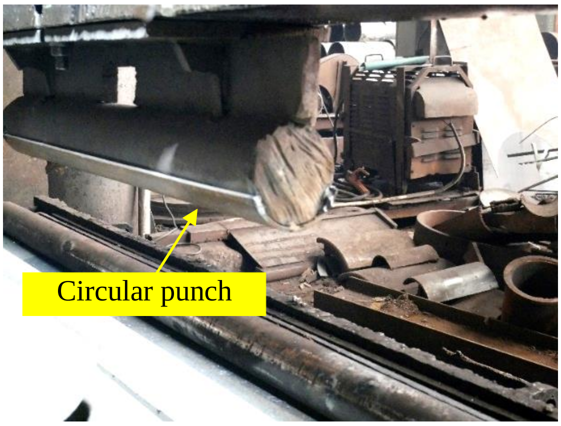

a) Press-braking for edge bending

b) Edge bending completed

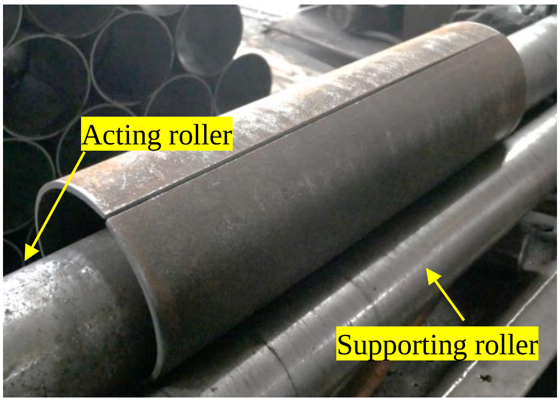

c) Transverse bending with a three-roller bending process

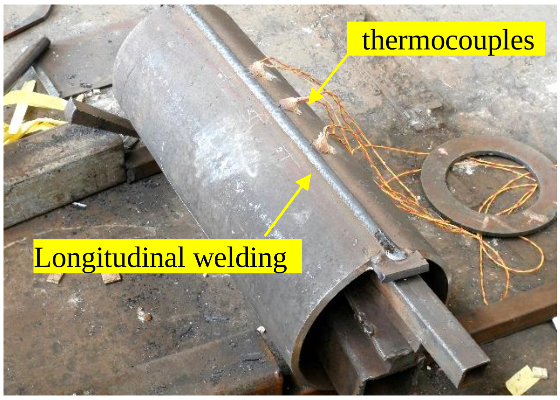

d) Longitudinal welding after transverse bending

Figure 2 Fabrication processes of CFCHS

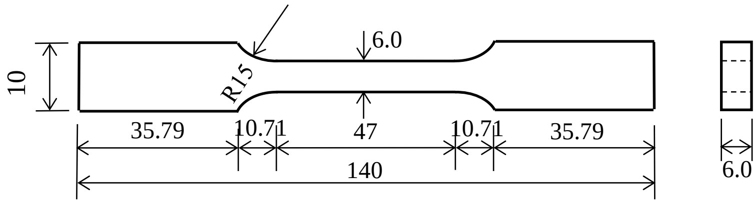

Note: All dimensions in millimeters (mm).

a) Geometry of standard tensile coupons

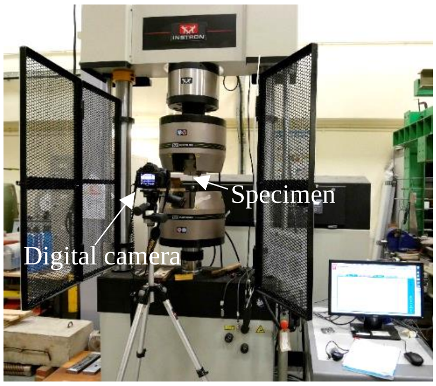

b) Test setup

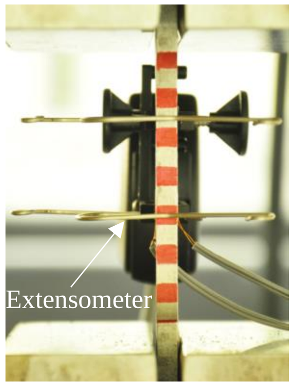

c) A coupon under testing

Figure 3 Standard tensile tests on S690 steels

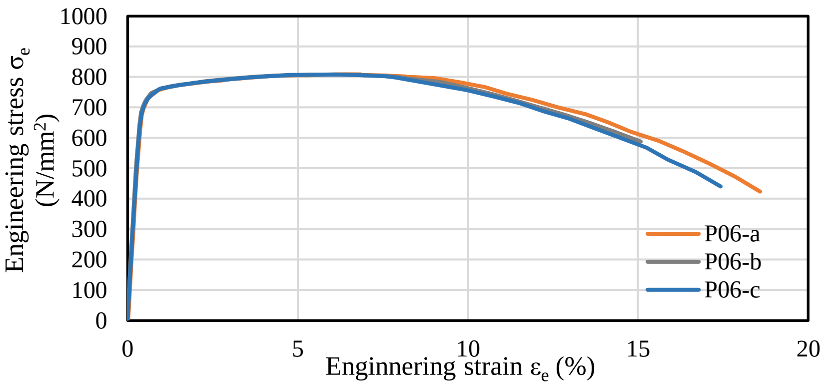

a) Measured engineering stress-strain ($\sigma_e - \varepsilon_e$) curves

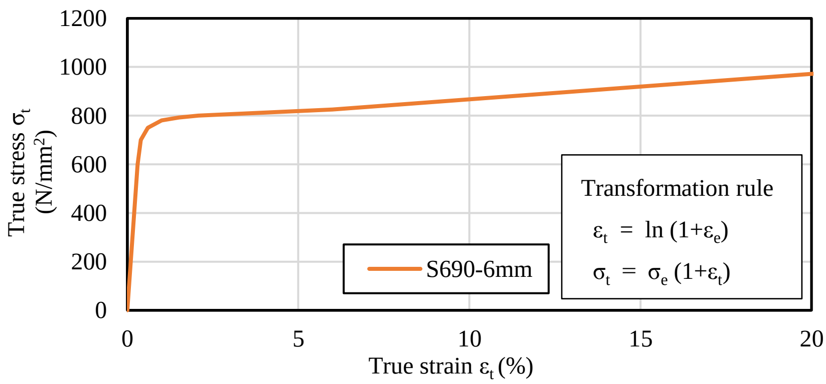

b) Transformed true stress-strain ($\sigma_t - \varepsilon_t$) curve

Figure 4 Stress-strain curves of S690 steels

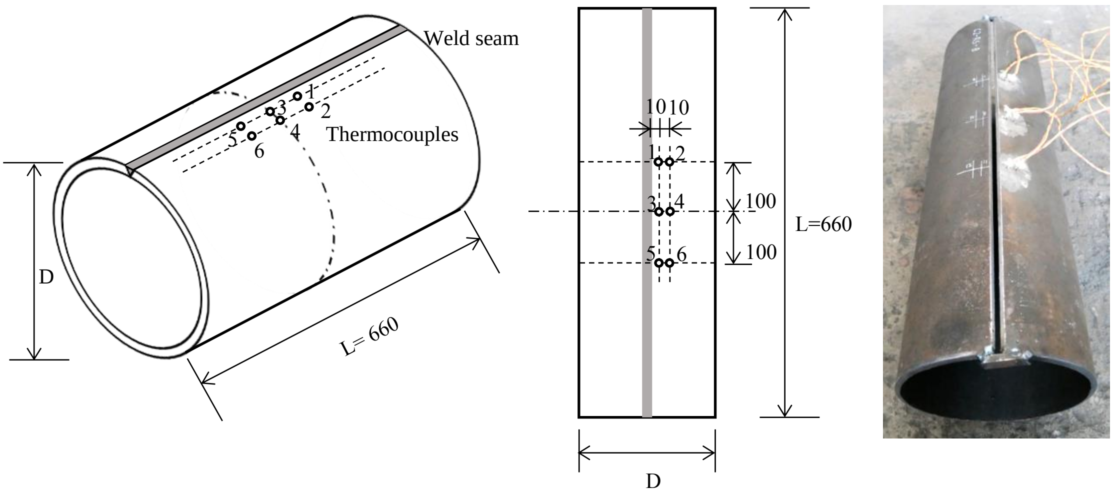

Figure 5　Setup of temperature measurement

Section C2

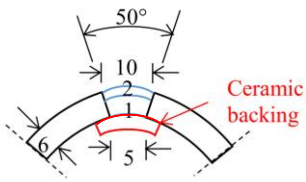

Weld seams for Sections C1 and C2

Figure 6　Detail of weld seams

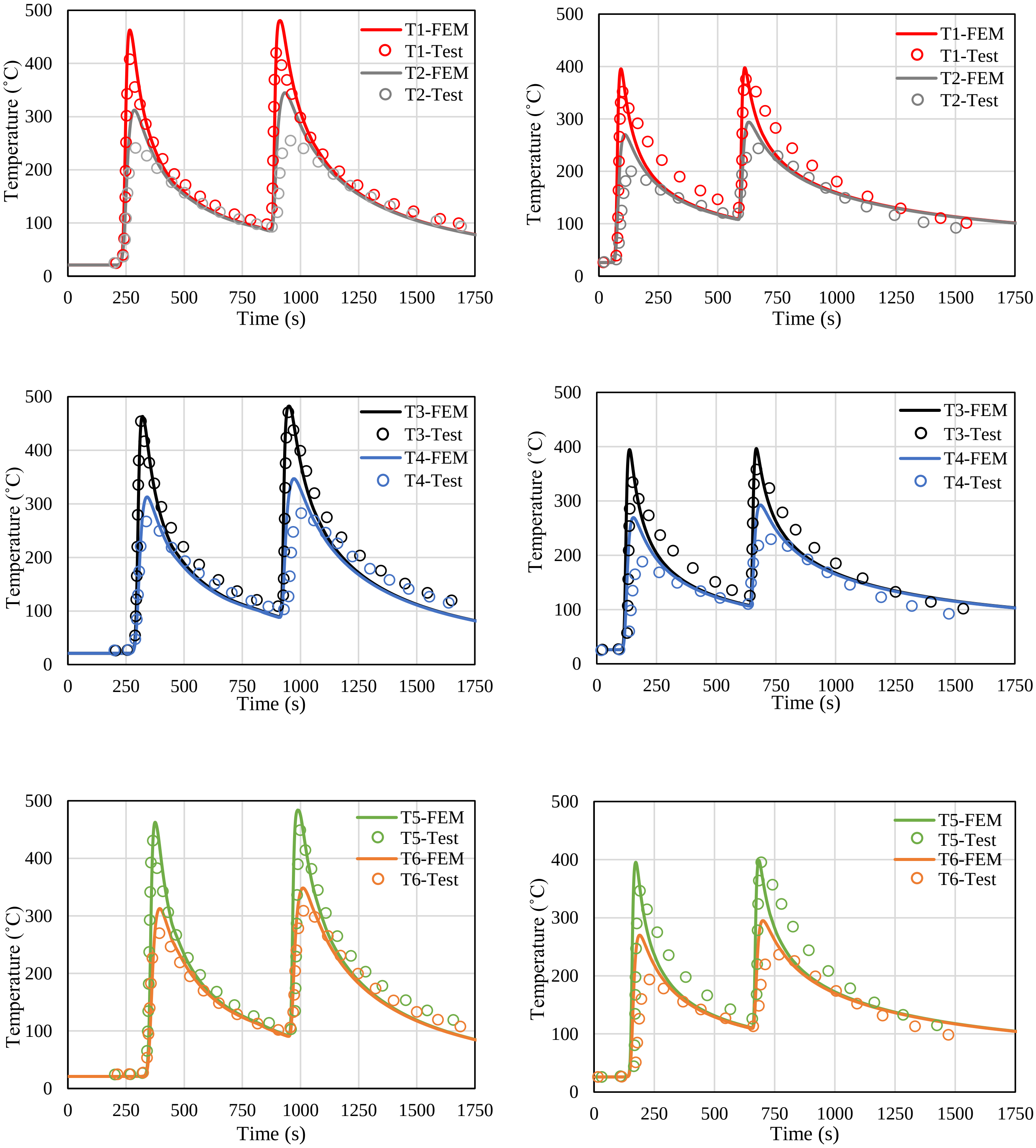

a) Section C1 **b) Section C2**

Figure 7 Temperature history at specific locations of Sections C1 and C2 during welding

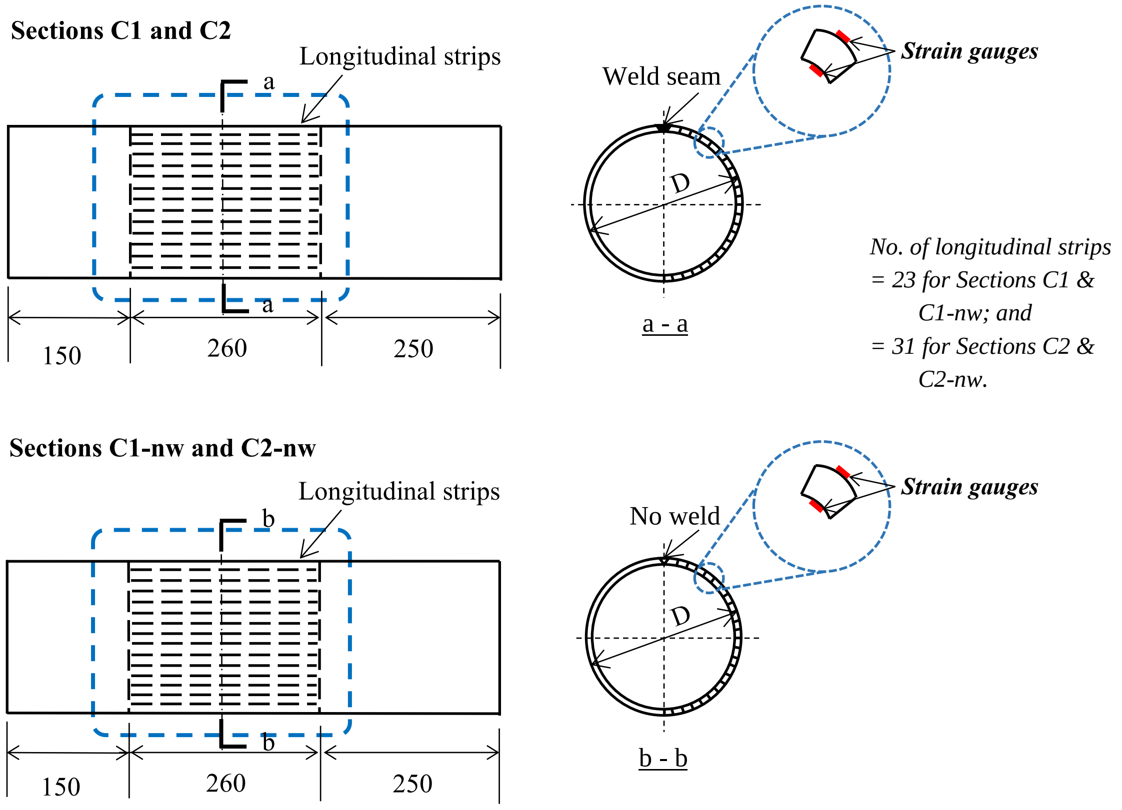

Figure 8 Details of sectioning and arrangement of strain gauges

a) Section C1-nw

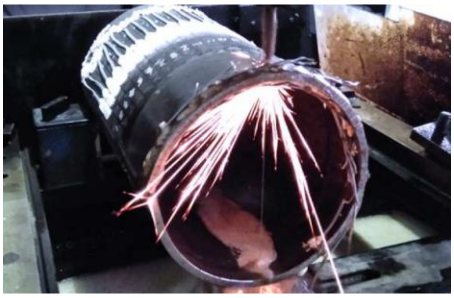

b) Wire cutting

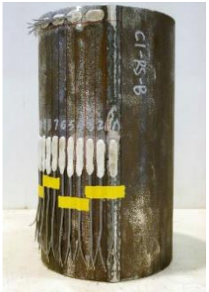

c) Section C1

d) Deformed steel strips cut from Section C1-nw

e) Deformed steel strips cut from Section C1

Figure 9 Sectioning method for residual stress measurement

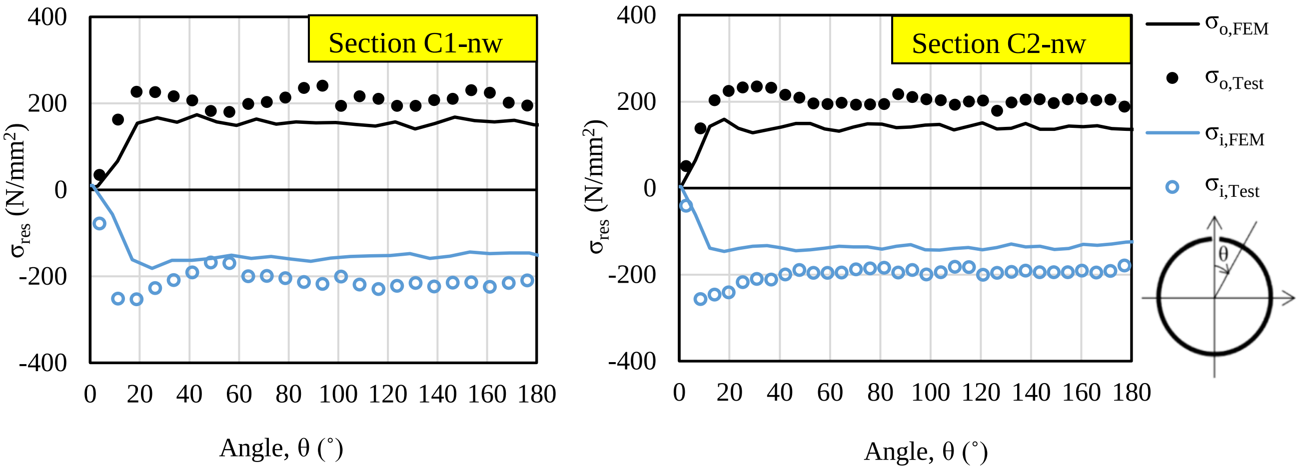

a) Transverse bending

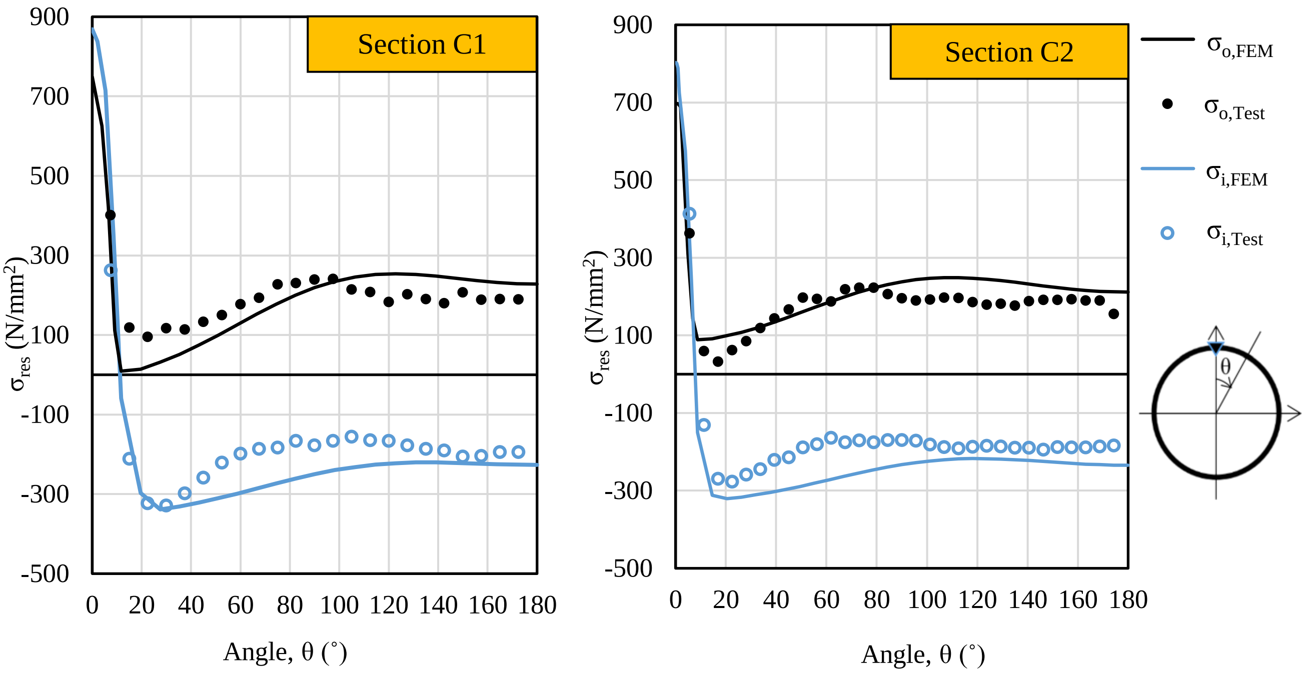

b) Transverse bending and longitudinal welding

Figure 10 Measured and predicted surface residual stresses of CFCHS

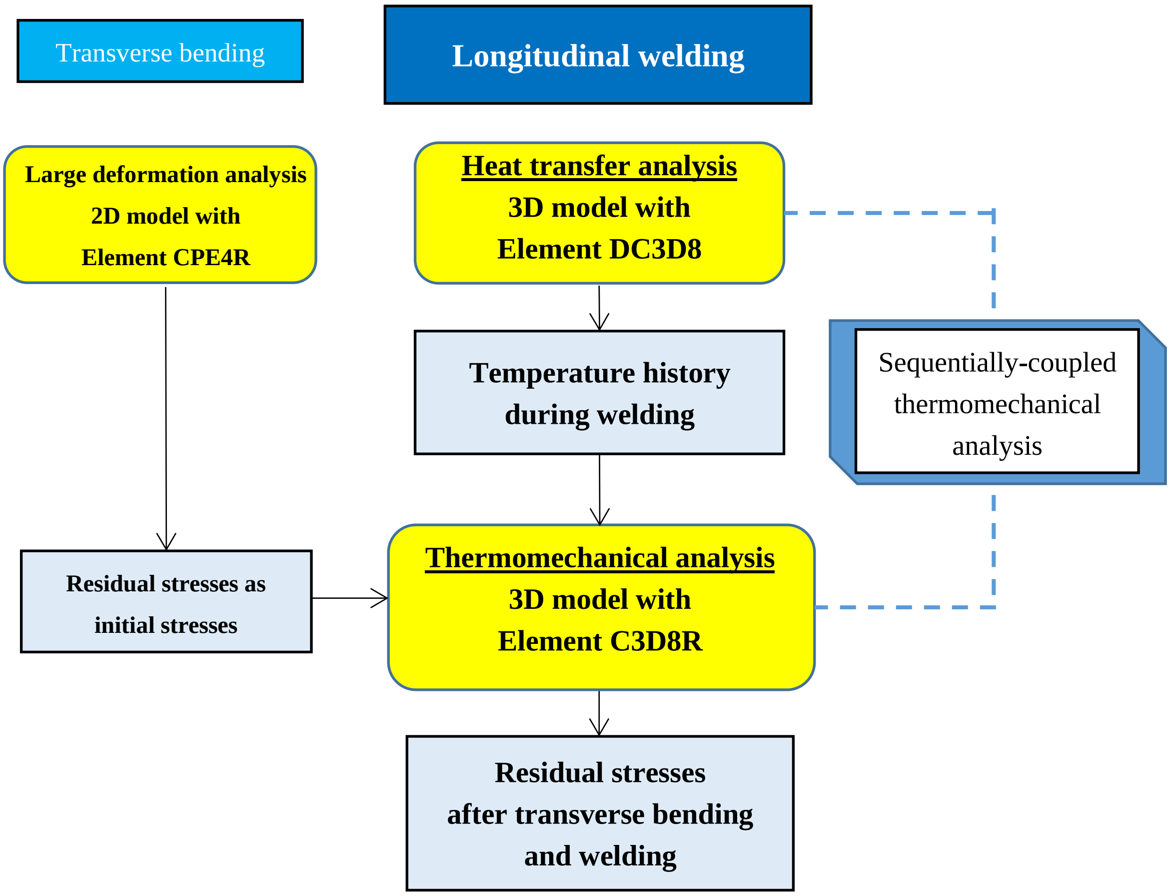

Figure 11 Flowchart of numerical prediction for residual stresses

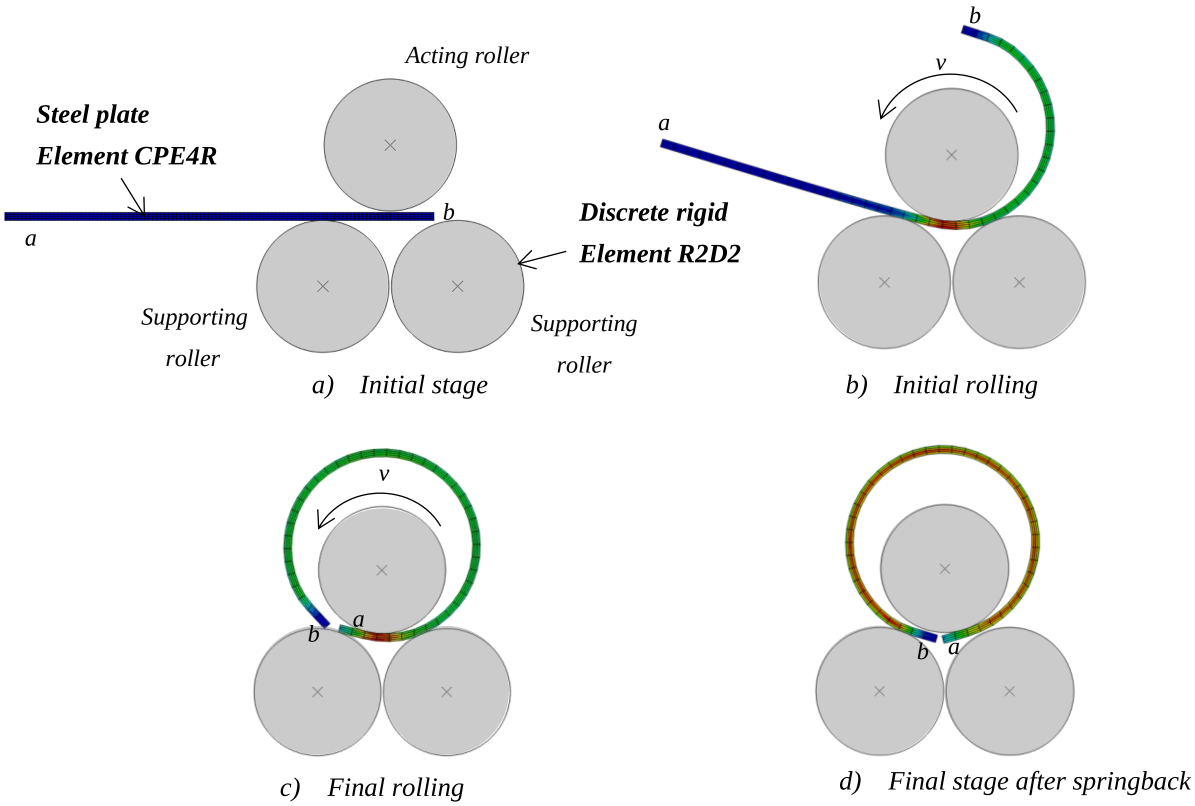

Figure 12 Finite element modelling of transverse bending

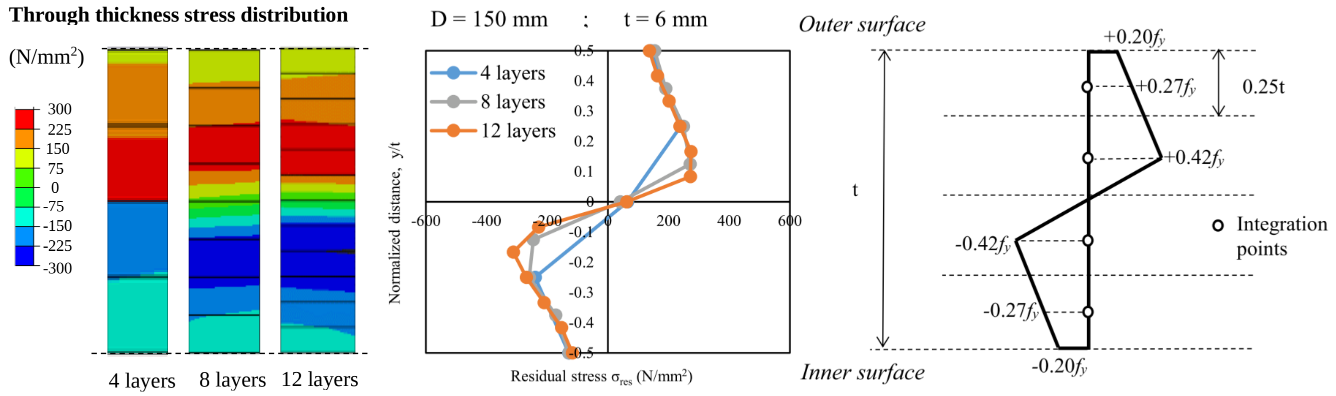

a) Longitudinal residual stresses

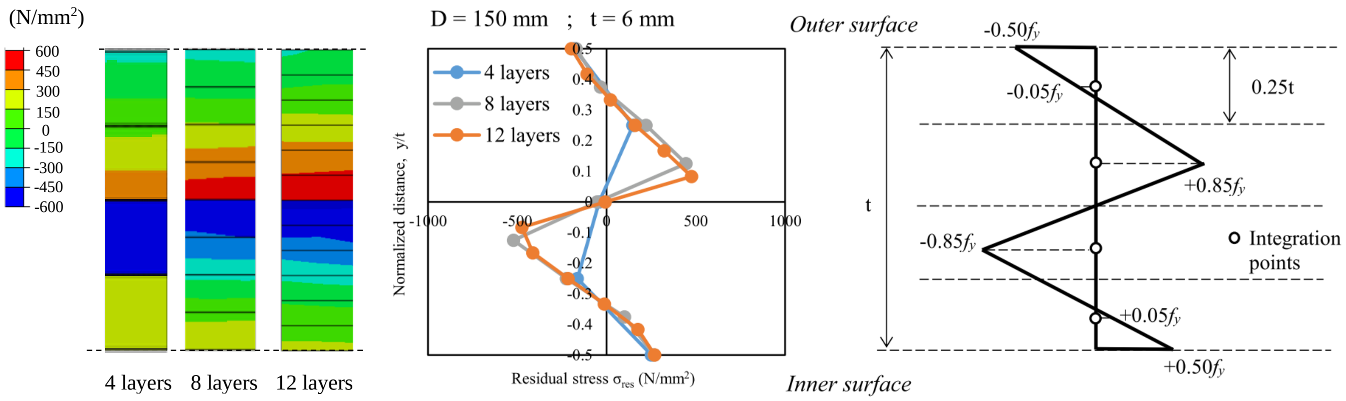

b) Transverse residual stresses

Figure 13 Mesh convergence studies for modelling of transverse bending

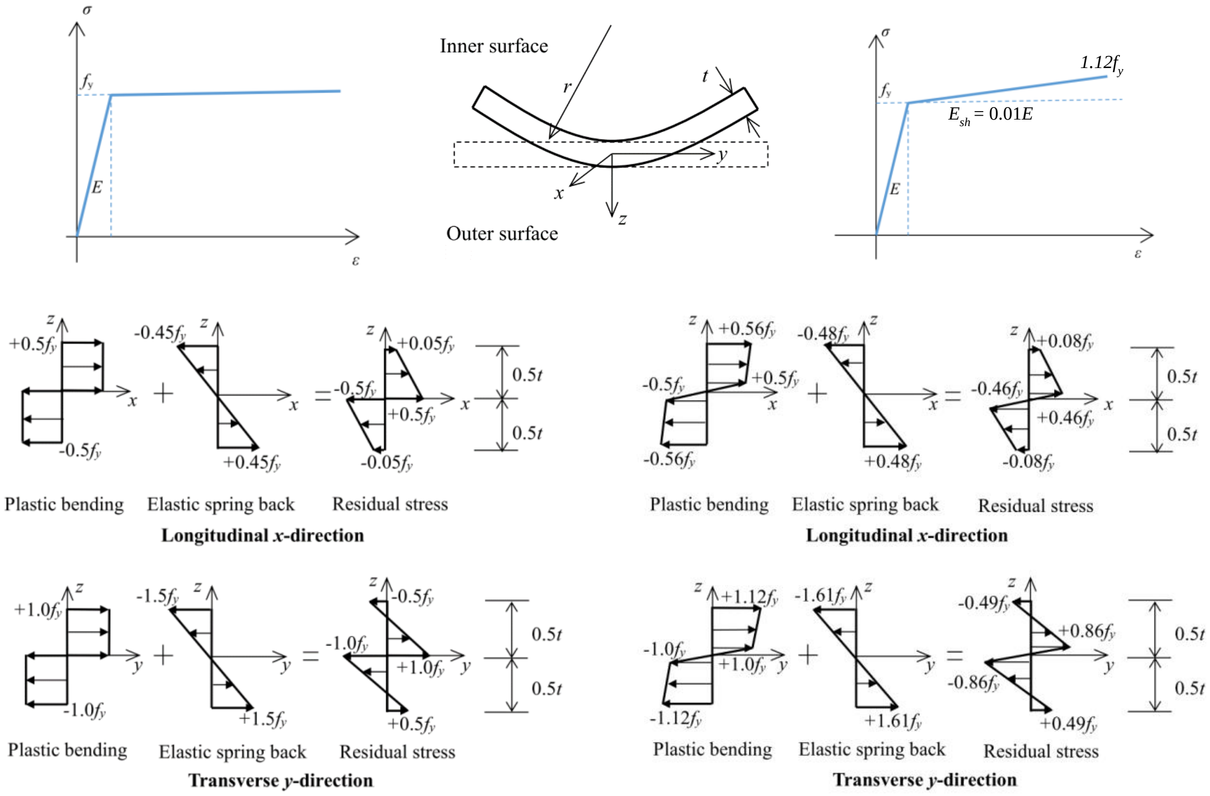

a) Moen et al. (2008) b) Hu (2019)

Figure 14 Analytical model of residual stresses induced by transverse bending

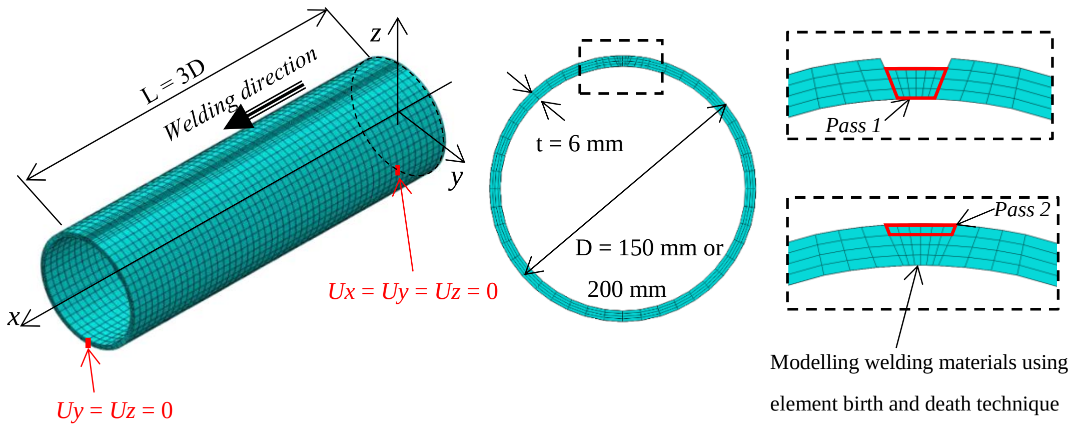

Figure 15 Finite element model of CFCHS for coupled thermomechanical analysis

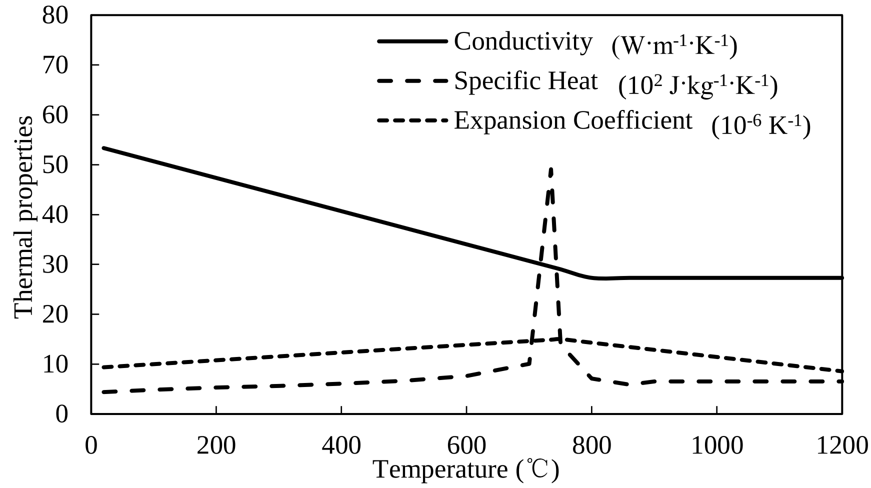

a) Thermal properties

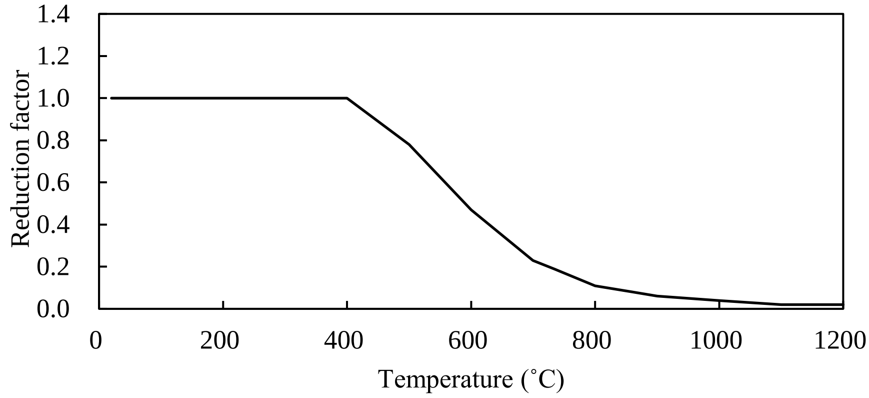

b) Reduction factors for yield strength

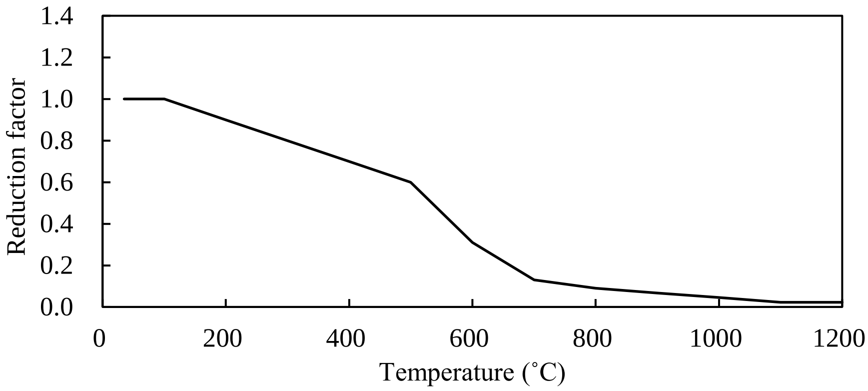

c) Reduction factor for Young's modulus

Figure 16 Thermal and mechanical properties of S690 steels at elevated temperatures

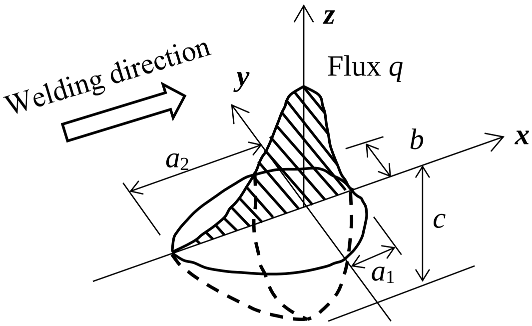

Parameters adopted for Sections C1 and C2

a_1 = 7.5 mm

a_2 = 10.0 mm

b = 5.0 mm

c = 10.0 mm

Figure 17 A double ellipsoidal model as a welding heat source

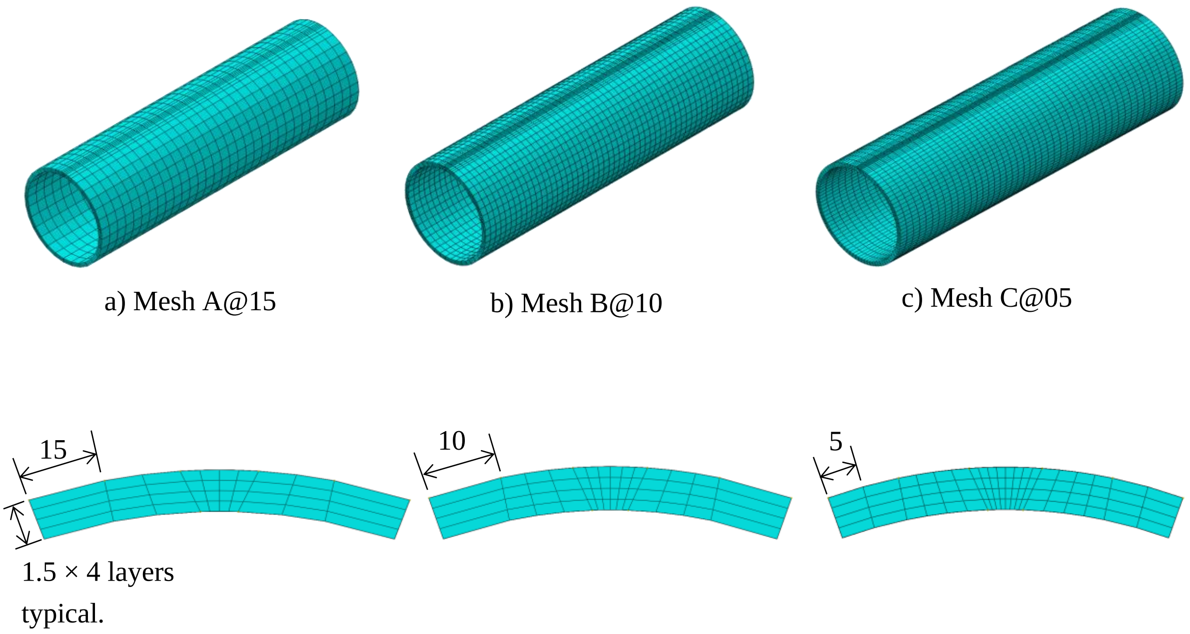

Figure 18 Mesh convergence study for modelling of longitudinal welding – Section C1

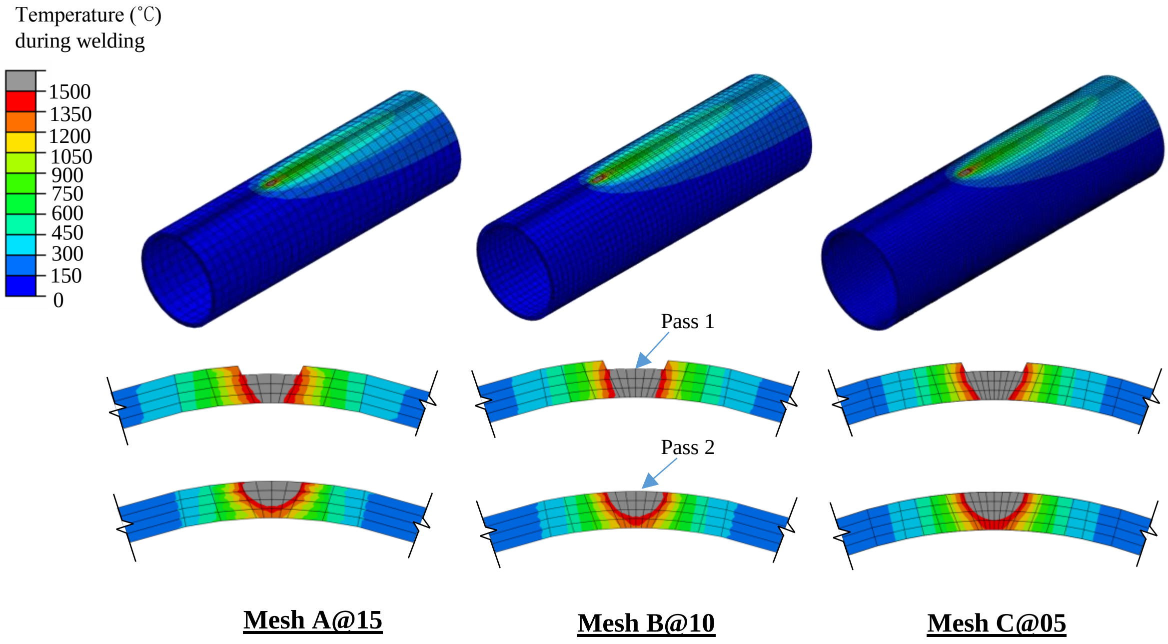

Predicted temperature during welding

a) Heat transfer analysis

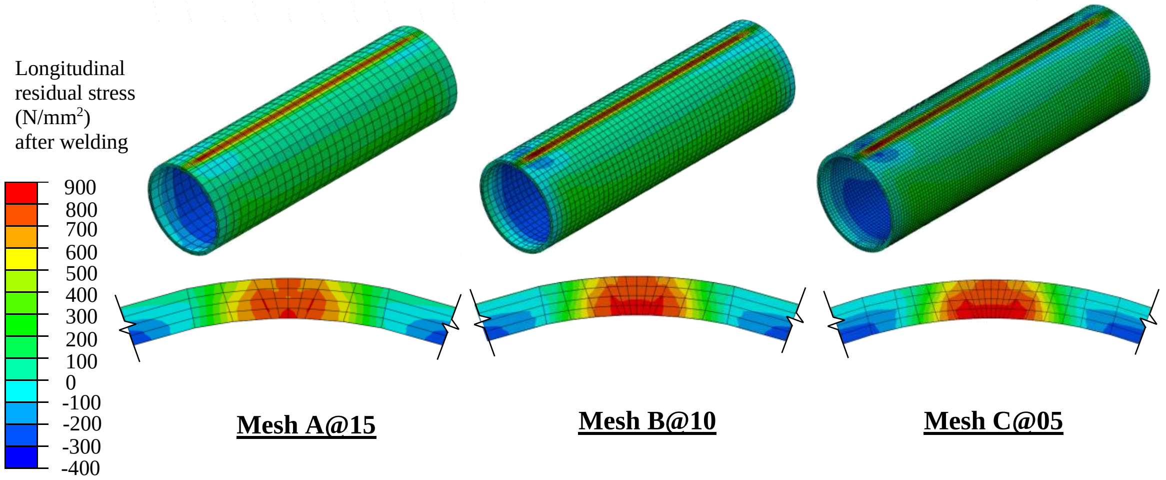

Predicted residual stresses after welding

b) Thermomechanical analysis

Figure 19 Temperature and residual stress distributions in the vicinity of welding seam of Section C1

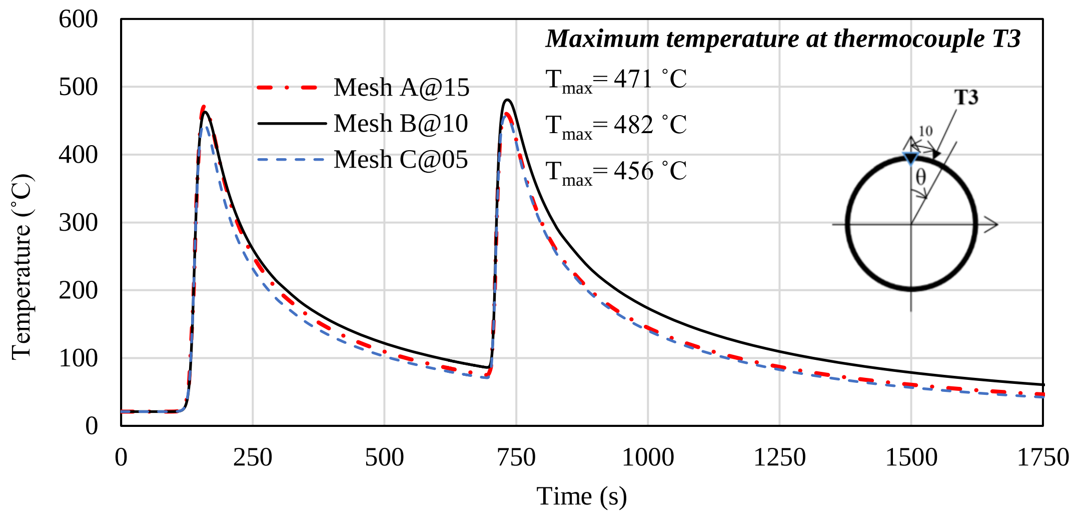

a) Temperature history

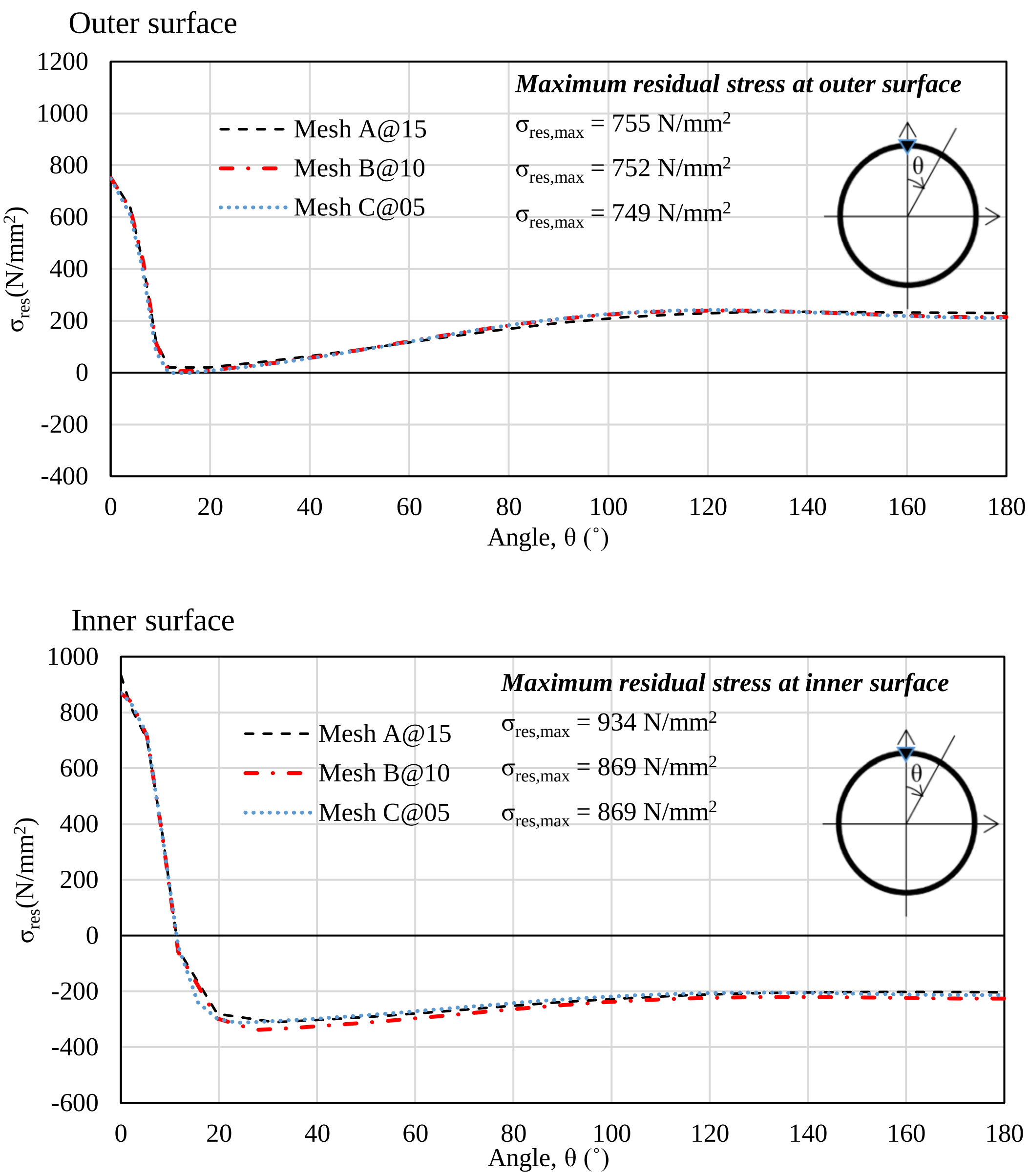

b) Residual stresses

Figure 20 Mesh convergence study on modelling of longitudinal welding

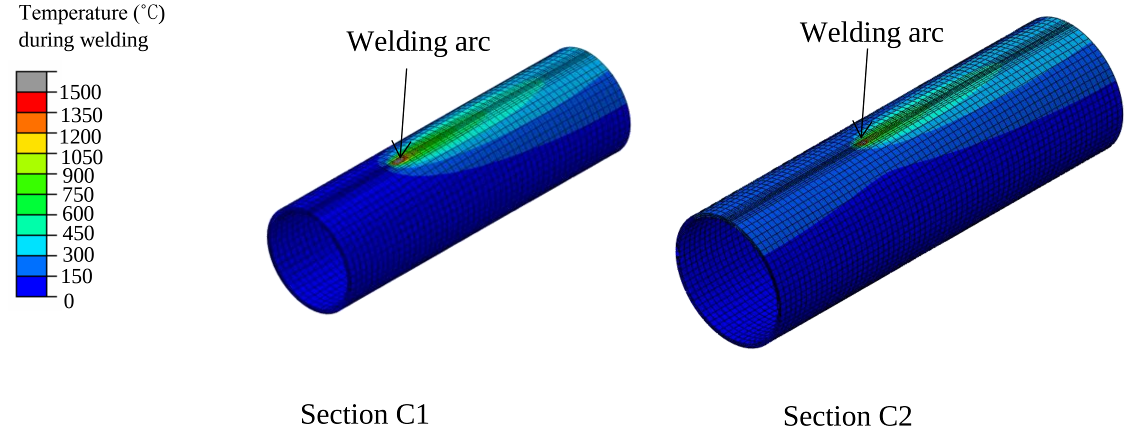

Predicted surface temperature during welding
a) Heat transfer analysis

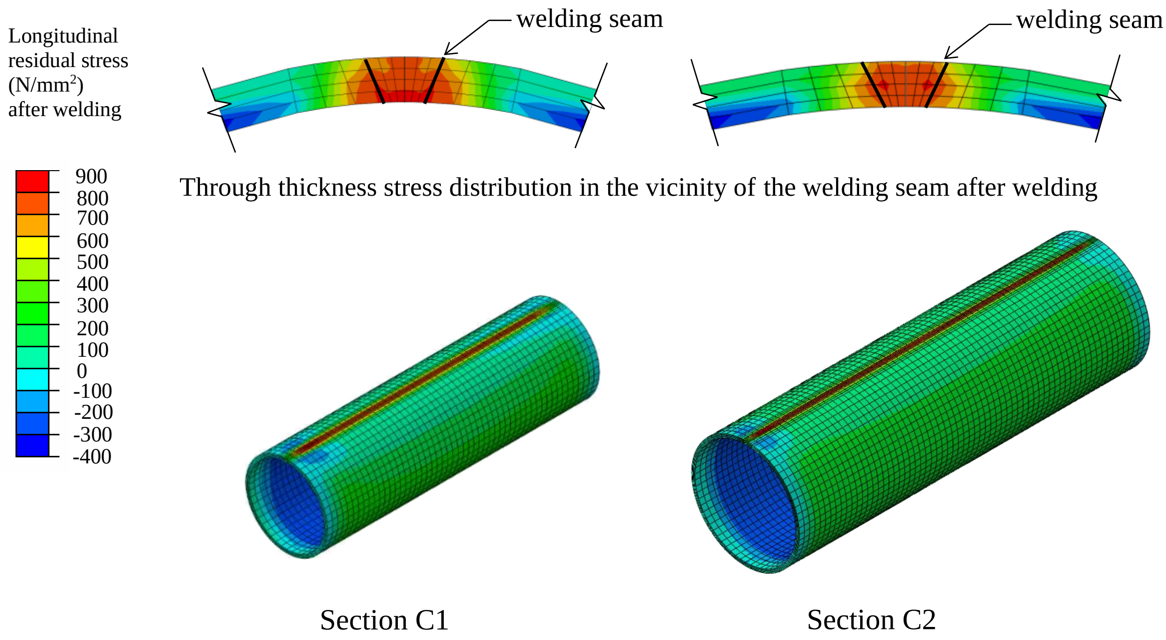

Predicted surface residual stresses after welding
b) Thermomechanical analysis

Figure 21 Typical numerical results for sequentially coupled thermomechanical analysis

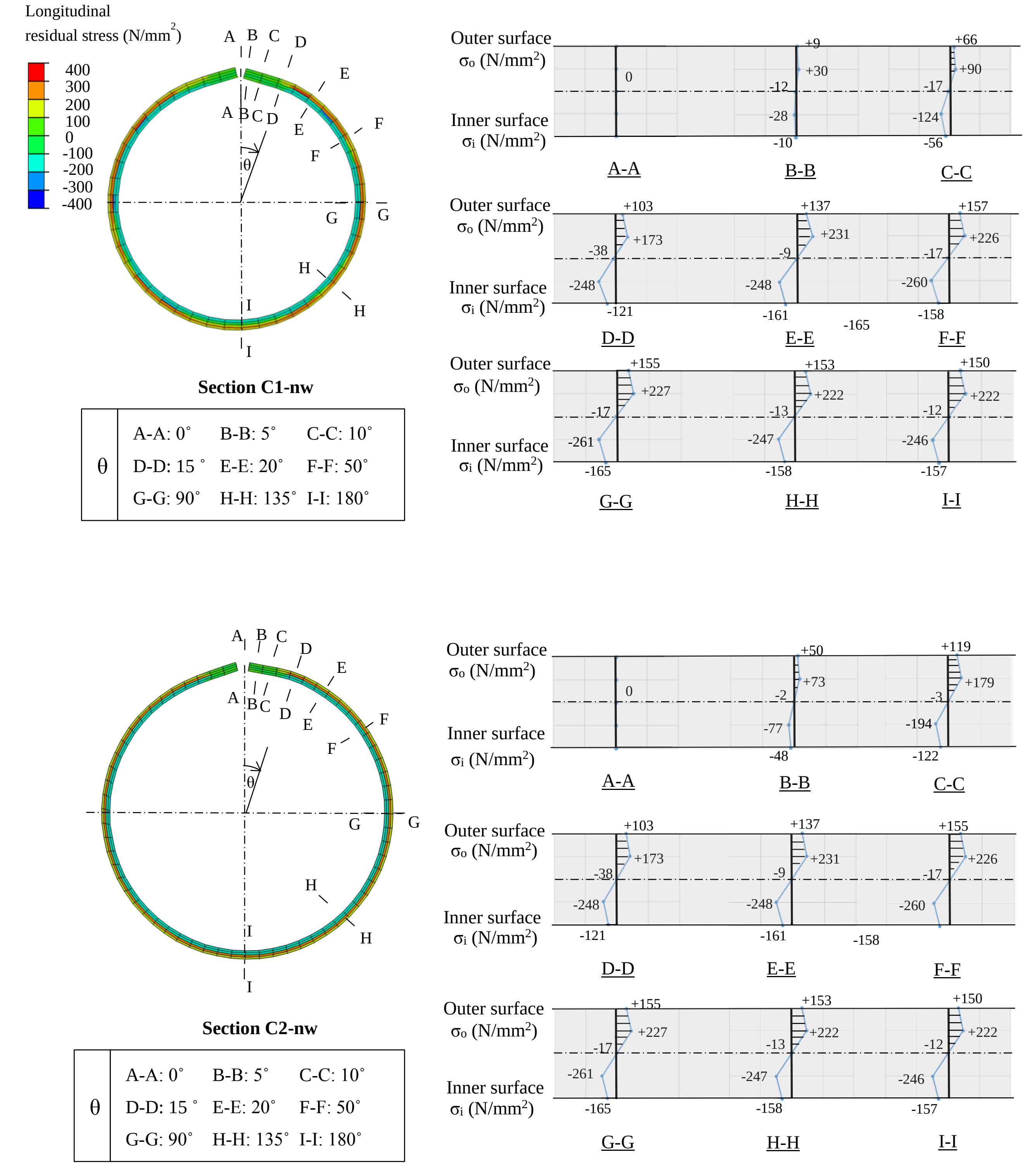

Figure 22 Longitudinal residual stress distributions of Sections C1-nw and C2-nw

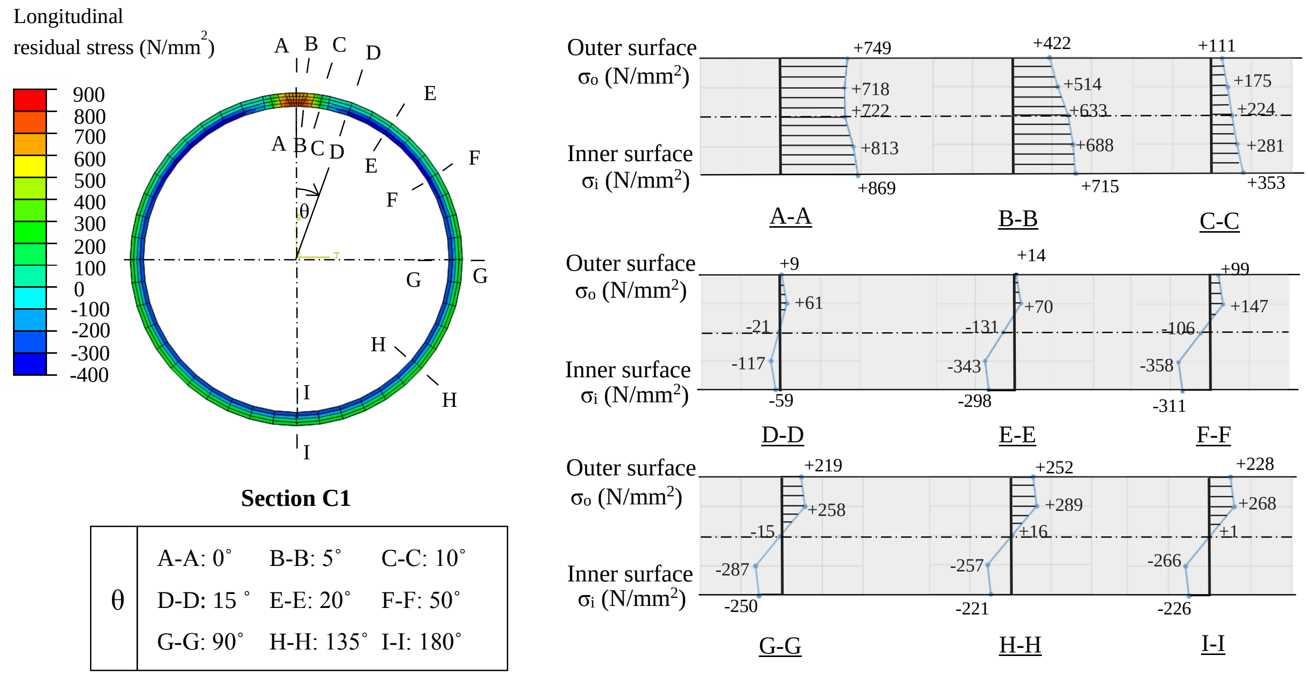

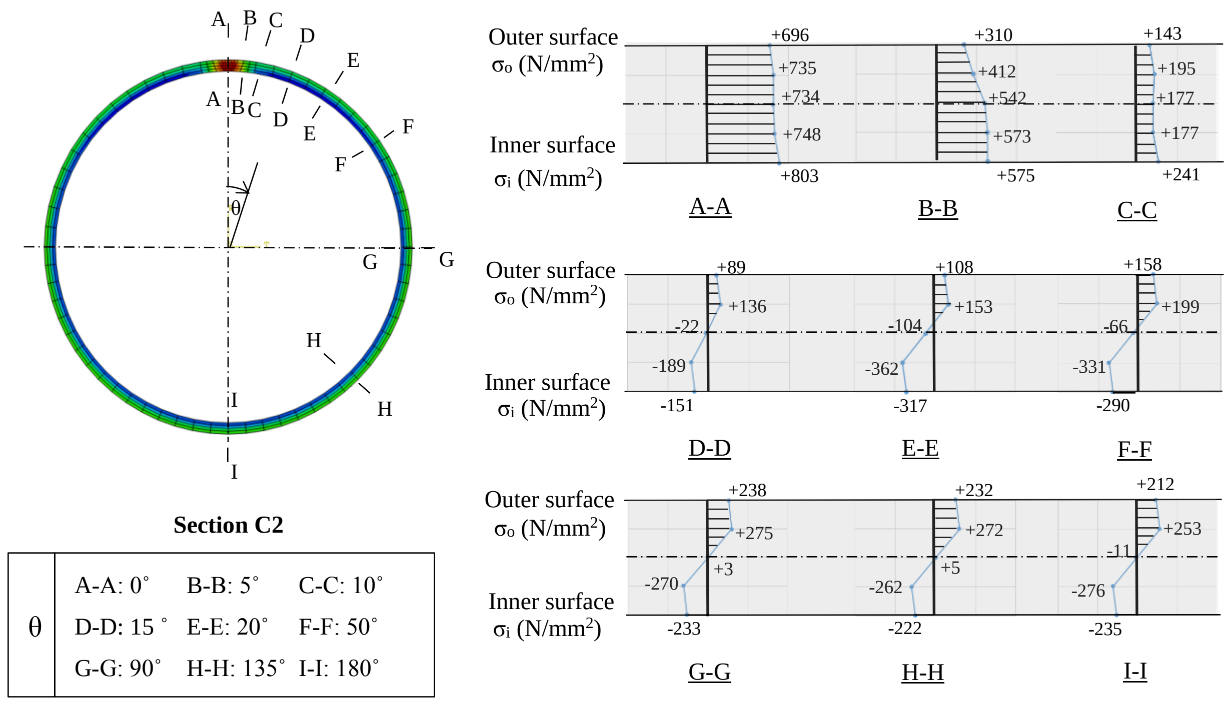

Figure 23 Longitudinal residual stress distributions of Sections C1 and C2

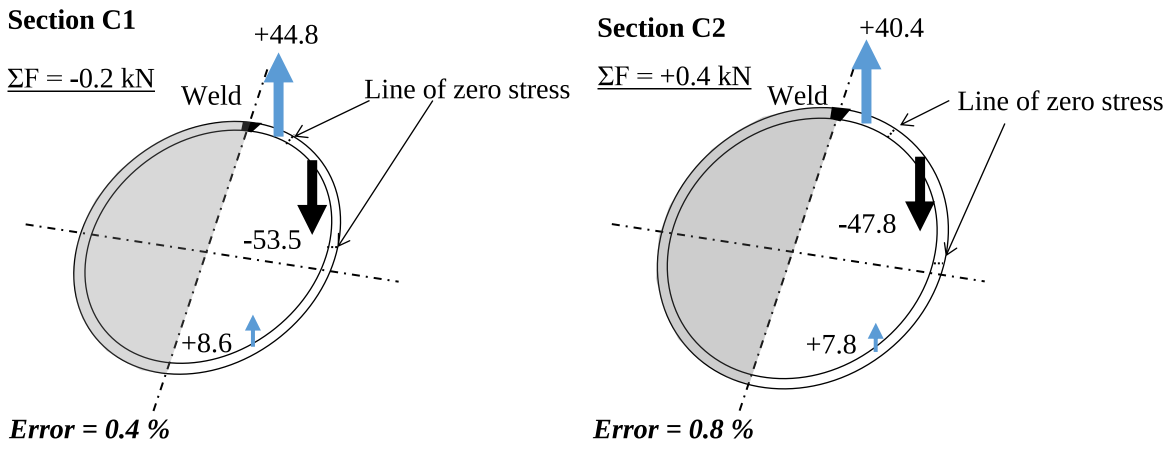

Figure 24 Force equilibrium in Sections C1 and C2

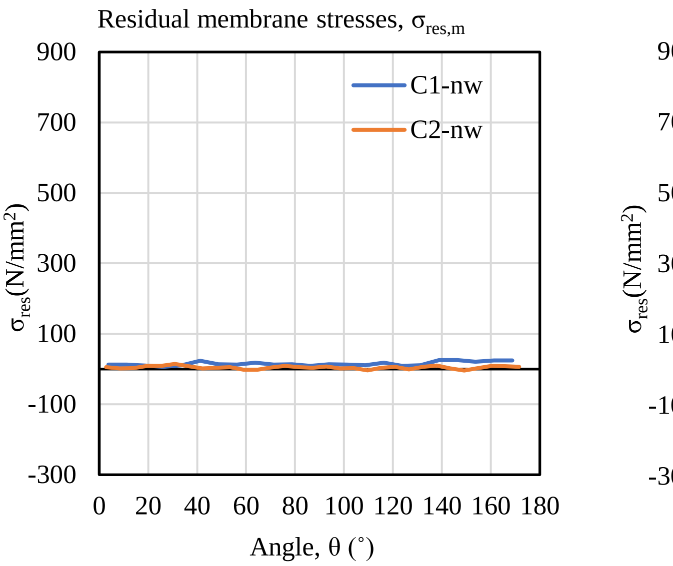

a) Residual membrane stresses of Sections C1-nw and C2-nw

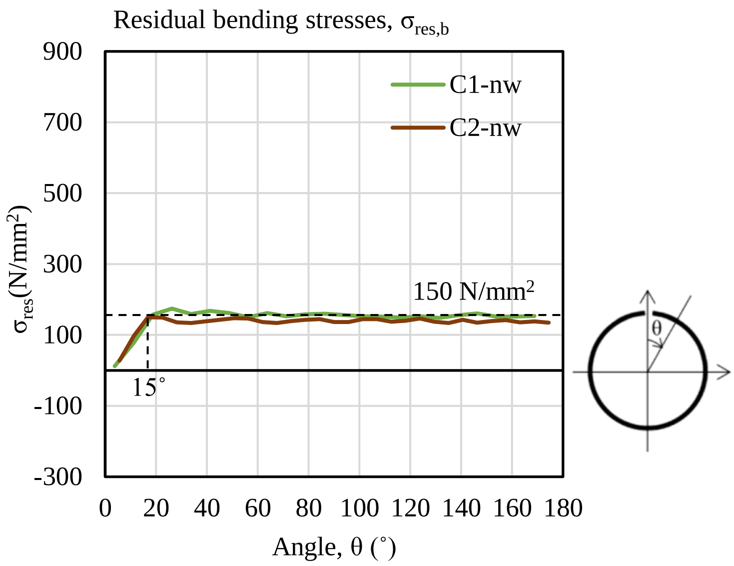

b) Residual bending stresses of Sections C1-nw and C2-nw

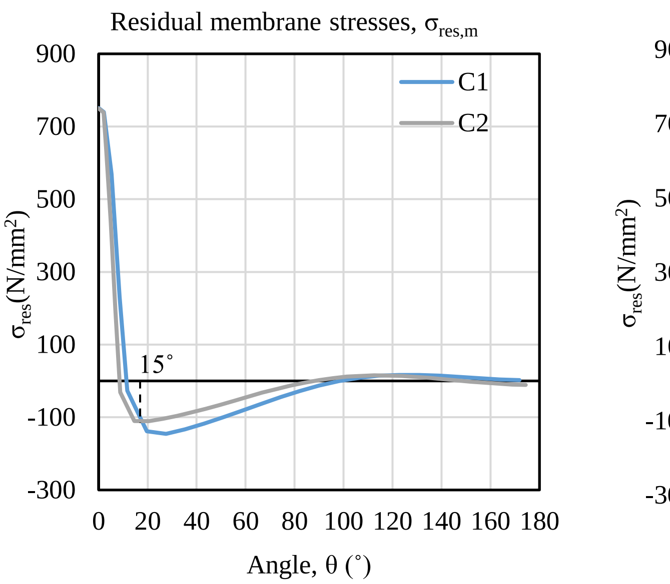

c) Residual membrane stresses of Sections C1 and C2

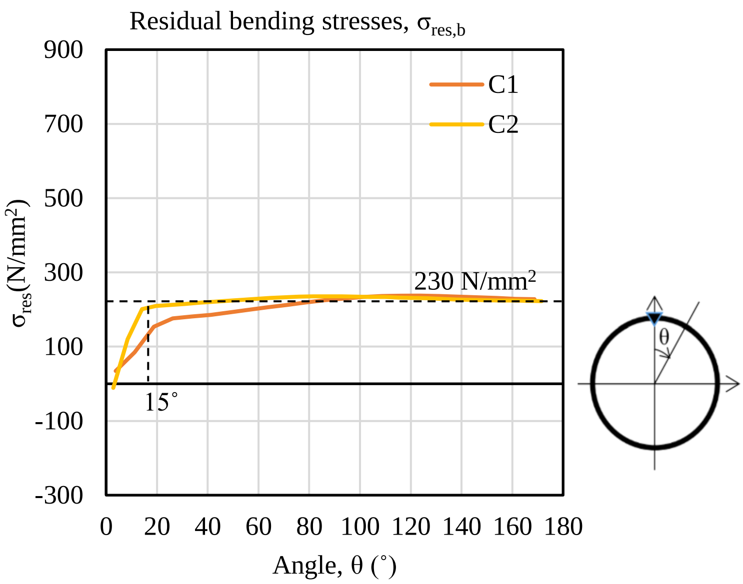

d) Residual bending stresses of Sections C1 and C2

Figure 25 Analysis on residual membrane and bending stresses

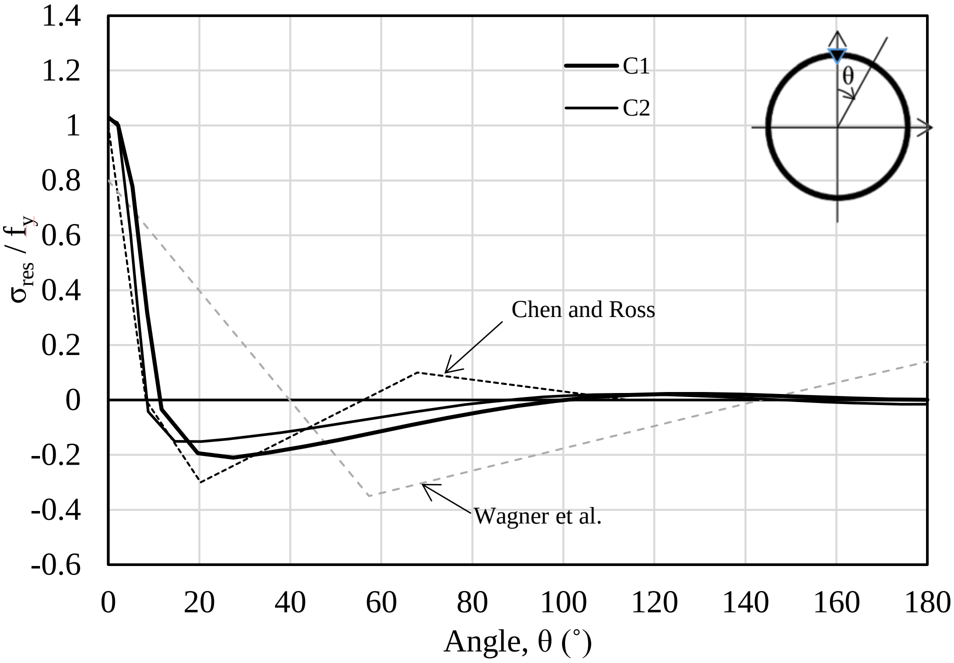

a) Residual stress patterns for S250 and S355 CFCHS

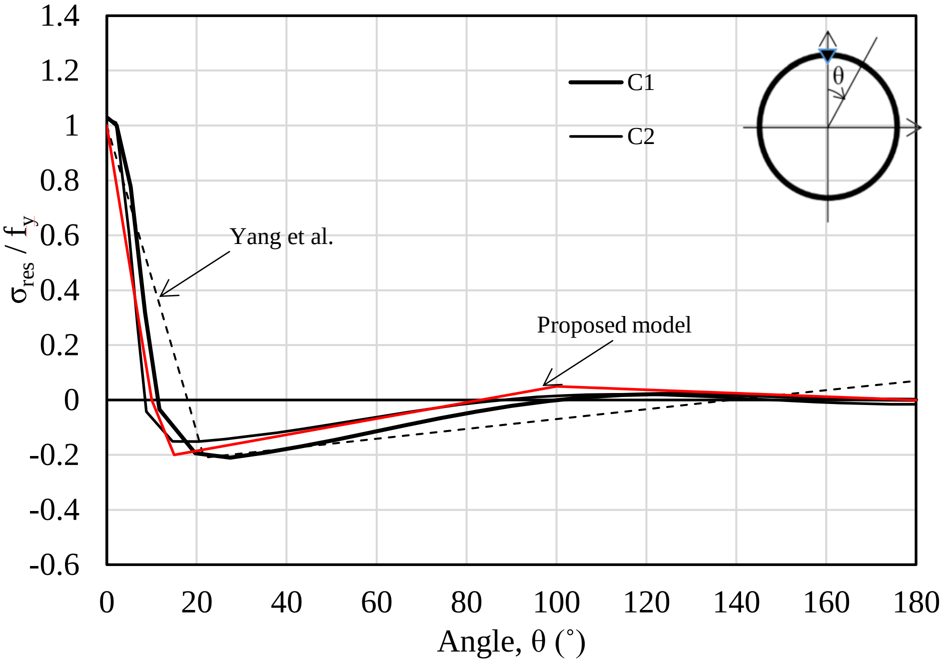

b) Residual stress patterns for S690 CFCHS

Figure 26 Comparison of test results and existing residual stress patterns

Table 1 Research programme and scope of work

Section D × t (mm×mm)	Fabrication process		Experimental measurements		Numerical modelling		
	Transverse bending	Longitudinal welding	Temperatures	Residual stresses	Transverse bending	Heat transfer	Thermomechanical analysis
C1-nw 150 × 6	**Y**	**---**	**---**	**Y**	**Y**	**---**	**---**
C1 150 × 6	**Y**	**Y**	**Y**	**Y**	**Y**	**Y**	**Y**
C2-nw 200 × 6	**Y**	**---**	**---**	**Y**	**Y**	**---**	**---**
C2 200 × 6	**Y**	**Y**	**Y**	**Y**	**Y**	**Y**	**Y**

Table 2 Materials specifications of S690 steel plates and welding electrode

Chemical compositions (%)

Material		**C**	**Mn**	**Si**	**S**	**P**	**Cr**	**Ni**	**Mo**	**Cu**
S690 steel plate	-	0.132	1.38	0.25	0.001	0.010	0.28	0.04	0.24	0.47
Welding electrode	Bohler GM 110	0.090	1.70	0.70	0.012	0.015	0.30	1.85	0.60	0.10

Table 3 Mechanical properties of S690 steel plates and welding electrode

No.	Young's modulus E (kN/mm2)	Yield strength f_y (N/mm2)	Tensile strength f_u (N/mm^2)	f_u / f_y	Strain at tensile strength ε_u (%)	Elongation at fu ≥ 15 (f_y / E)	Elongation at fracture ε_f (%)
EN 10025-6	—	*690*	*770~940*	*1.05*	—	—	*14%*
P06-1	202	729	809	1.11	6.8	Y	18.6
P06-2	201	728	808	1.11	5.8	Y	15.1
P06-3	204	722	808	1.12	6.1	Y	17.4
Average	**202**	**726**	**808**	**1.11**	**6.2**	**—**	**17.0**
Bohler GM 110	—	720	880	1.22	—	—	15.0

Table 4 Welding parameters for GMAW

Section	Weld pass	Current I (A)	Voltage U (V)	Welding speed v (mm/s)	Welding efficiency η	Line heat input energy q (kJ/mm)
C1	1	135-150	18.2	1.84	0.85	1.14 ~ 1.26
	2	175-185	21.2	2.81	0.85	1.12 ~ 1.19
C2	1	165-180	19.5	2.40	0.85	1.14 ~ 1.24
	2	166-185	21.1	3.25	0.85	0.92 ~ 1.02

Note: Line heat input energy $q = \eta \times \frac{I \times U}{v}$

Table 5 Measured and predicted maximum temperatures during welding

Section C1	Temperature (ºC) Pass 1			Temperature (ºC) Pass 2		
	T_m	T_p	$T_p - T_m$	T_m	T_p	$T_p - T_m$
T1	409	463	54	425	482	57
T3	454		9	473		9
T5	431		32	449		33
		Average	32		Average	33
			6.9%			6.8%
T2	241	313	71	255	347	90
T4	268		45	283		64
T6	270		43	309		39
		Average	53		Average	64
			16.9%			18.4%

Section C2	Temperature (ºC) Pass 1			Temperature (ºC) Pass 2		
	T_m	T_p	$T_p - T_m$	T_m	T_p	$T_p - T_m$
T1	352	395	43	376	398	22
T3	335		60	358		39
T5	346		49	395		4
		Average	51		Average	22
			12.9%			5.5%
T2	200	270	70	244	294	50
T4	188		81	229		64
T6	194		76	236		59
		Average	76		Average	58
			28.1%			19.7%

Table 6 Longitudinal residual stresses of Section C1-nw (D/t = 25.0)

	Inner residual stress			Outer residual stress		
Point	$\sigma_{i,Test}$ (N/mm^2)	$\sigma_{i,FEM}$ (N/mm^2)	$\Delta\sigma_i = \sigma_{i,FEM} - \sigma_{i,Test}$	$\sigma_{o,Test}$ (N/mm^2)	$\sigma_{o,FEM}$ (N/mm^2)	$\Delta\sigma_o = \sigma_{o,FEM} - \sigma_{o,Test}$
1	-78	-13	-	35	-	-
2	-252	-70	-	162	-	-
3	-253	-161	-	227	-	-
4	-227	-182	45	226	167	-59
5	-209	-163	46	217	156	-61
6	-191	-163	28	206	174	-32
7	-168	-158	10	182	166	-16
8	-170	-151	19	180	149	-31
9	-200	-159	41	199	164	-35
10	-199	-154	45	203	152	-51
11	-205	-160	45	213	156	-57
12	-213	-165	48	235	155	-80
13	-217	-158	59	241	155	-86
14	-201	-154	47	194	151	-43
15	-219	-153	66	216	151	-65
16	-229	-152	77	210	147	-63
17	-222	-148	74	194	157	-37
18	-216	-156	60	194	141	-53
19	-224	-158	66	207	153	-54
20	-215	-153	62	210	168	-42
21	-214	-143	71	230	160	-70
22	-224	-147	77	225	157	-68
23	-216	-146	70	201	161	-40
Average	-209	-156	53	209	157	-52
	$\frac{\text{Average } \Delta\sigma_i}{\text{Average } \sigma_{i,Test}}$		25 %	$\frac{\text{Average } \Delta\sigma_o}{\text{Average } \sigma_{o,Test}}$		25 %
	$\frac{\text{Average } \Delta\sigma_i}{f_y}$		7.3 %	$\frac{\text{Average } \Delta\sigma_o}{f_y}$		7.2 %

Note: $f_y = 726\ N/mm^2$

Table 7 Longitudinal residual stresses of Section C2-nw (D/t = 33.3)

	Inner residual stress			Outer residual stress		
Point	$\sigma_{i,Test}$ (N/mm^2)	$\sigma_{i,FEM}$ (N/mm^2)	$\Delta\sigma_i$ $= \sigma_{i,FEM} - \sigma_{i,Test}$	$\sigma_{o, Test}$ (N/mm^2)	$\sigma_{o, FEM}$ (N/mm2)	$\Delta\sigma_o$ $= \sigma_{o,FEM} - \sigma_{o,Test}$
1	-41	-27	-	159	28	-
2	-257	-96	-	138	99	-
3	-247	-146	-	203	124	-
4	-241	-139	102	224	159	-65
5	-218	-134	84	233	138	-95
6	-211	-133	78	234	135	-99
7	-212	-135	77	231	141	-90
8	-200	-140	60	215	145	-70
9	-190	-145	45	209	149	-60
10	-197	-143	54	195	150	-45
11	-196	-136	60	194	137	-57
12	-196	-135	61	196	132	-64
13	-189	-136	53	192	142	-50
14	-186	-138	48	193	148	-45
15	-185	-141	44	194	148	-46
16	-196	-134	62	217	140	-77
17	-190	-131	59	210	142	-68
18	-200	-143	57	205	146	-59
19	-195	-143	52	203	147	-56
20	-182	-140	42	192	135	-57
21	-183	-137	46	200	143	-57
22	-201	-142	59	202	151	-51
23	-197	-138	59	178	137	-41
24	-194	-130	64	197	138	-59
25	-191	-136	55	204	149	-55
26	-195	-134	61	205	136	-69
27	-195	-142	53	196	136	-60
28	-195	-140	55	205	144	-61
29	-191	-130	61	206	142	-64
30	-195	-133	62	203	144	-59
31	-192	-132	60	204	138	-66
Average	-197	-137	60	205	143	-62
$\frac{\text{Average } \Delta\sigma_i}{\text{Average } \sigma_{i,Test}}$			30 %	$\frac{\text{Average } \Delta\sigma_o}{\text{Average } \sigma_{o,Test}}$		30 %
$\frac{\text{Average } \Delta\sigma_i}{f_y}$			8.3 %	$\frac{\text{Average } \Delta\sigma_o}{f_y}$		8.5 %

Note: f_y = 726 N/mm^2

Table 8 Longitudinal residual stresses of Section C1 (D/t = 25.0)

	Inner residual stress			Outer residual stress		
Point	$\sigma_{i,Test}$ (N/mm^2)	$\sigma_{i,FEM}$ (N/mm^2)	$\Delta\sigma_i = \sigma_{i,FEM} - \sigma_{i,Test}$	$\sigma_{o,Test}$ (N/mm^2)	$\sigma_{o,FEM}$ (N/mm^2)	$\Delta\sigma_o = \sigma_{o,FEM} - \sigma_{o,Test}$
1	262	353	91	400	422	22
2	-211	-59	152	118	111	-7
3	-323	-298	25	95	9	-86
4	-328	-339	-11	117	14	-103
5	-298	-331	-33	114	31	-83
6	-259	-321	-62	133	51	-82
7	-221	-311	-90	150	74	-76
8	-199	-299	-100	177	99	-78
9	-186	-286	-100	193	126	-67
10	-183	-273	-90	227	152	-78
11	-166	-261	-95	230	177	-53
12	-177	-250	-73	240	200	-40
13	-166	-240	-74	241	219	-22
14	-156	-232	-76	214	235	21
15	-165	-226	-61	208	246	38
16	-166	-222	-56	183	252	69
17	-177	-221	-44	203	254	51
18	-187	-220	-33	190	252	62
19	-190	-221	-31	180	248	68
20	-206	-223	-17	207	243	36
21	-204	-225	-21	189	237	48
22	-194	-226	-32	190	232	42
23	-194	-226	-32	190	229	39
Average	-182	-228	37	203	237	12
$\frac{\text{Average } \Delta\sigma_i}{\text{Average } \sigma_{i,Test}}$			21 %	$\frac{\text{Average } \Delta\sigma_o}{\text{Average } \sigma_{o,Test}}$		6 %
$\frac{\text{Average } \Delta\sigma_i}{f_y}$			5.1 %	$\frac{\text{Average } \Delta\sigma_o}{f_y}$		1.7 %

Note: f_y = 726 N/mm^2

Table 9 Longitudinal residual stresses of Section C2 (D/t = 33.3)

	Inner residual stress			Outer residual stress		
Point	$\sigma_{i,Test}$ (N/mm^2)	$\sigma_{i,FEM}$ (N/mm^2)	$\Delta\sigma_i = \sigma_{i,FEM} - \sigma_{i,Test}$	$\sigma_{o,Test}$ (N/mm^2)	$\sigma_{o,FEM}$ (N/mm^2)	$\Delta\sigma_o = \sigma_{o,FEM} - \sigma_{o,Test}$
1	413	575	162	362	553	191
2	-131	-151	-20	59	89	30
3	-270	-312	-42	32	91	59
4	-277	-321	-44	61	99	38
5	-259	-317	-58	85	108	23
6	-245	-311	-66	118	118	0
7	-221	-305	-84	143	131	-12
8	-214	-297	-83	166	144	-22
9	-189	-289	-100	197	158	-39
10	-181	-281	-100	193	172	-21
11	-164	-272	-108	187	186	-1
12	-176	-264	-88	218	199	-19
13	-171	-255	-84	222	211	-11
14	-176	-247	-71	222	222	0
15	-170	-240	-70	206	231	25
16	-170	-233	-63	195	238	43
17	-172	-228	-56	189	243	54
18	-182	-223	-41	192	247	55
19	-189	-220	-31	197	248	51
20	-191	-218	-27	196	249	53
21	-188	-218	-30	185	247	62
22	-185	-218	-33	179	245	66
23	-187	-219	-32	181	241	60
24	-190	-220	-30	176	237	61
25	-190	-222	-32	187	232	45
26	-195	-225	-30	191	228	37
27	-188	-227	-39	191	223	32
28	-189	-230	-41	193	219	26
29	-189	-232	-43	190	216	26
30	-186	-233	-47	189	214	25
31	-184	-234	-50	155	212	57
Average	-187	-224	48	186	233	32
	$\frac{\text{Average } \Delta\sigma_i}{\text{Average } \sigma_{i,Test}}$		26 %	$\frac{\text{Average } \Delta\sigma_o}{\text{Average } \sigma_{o,Test}}$		17 %
	$\frac{\text{Average } \Delta\sigma_i}{f_y}$		6.6 %	$\frac{\text{Average } \Delta\sigma_o}{f_y}$		4.4 %

Note: f_y = 726 N/mm^2

Table 10 Convergence study on mesh configurations

	Global mesh size (mm)	Local mesh size at weld groove (mm)	Nos. of elements			Total nos. of elements	Computational time (hour)
			Along perimeter	Across thickness	Along length		
Mesh A	15	2	40	4	42	6720	29.1
Mesh B	10	2	54	4	68	14,688	47.7
Mesh C	5	1	96	6	132	76,032	164.6